UCRL-11149

University of California

Ernest O. Lawrence Radiation Laboratory

TWO-WEEK LOAN COPY

This is a Library Circulating Copy which may be borrowed for two weeks. For a personal retention copy, call Tech. Info. Division, Ext. 5545

SCATTERING OF 250-MeV POSITIVE PI MESONS FROM A POLARIZED PROTON TARGET

Berkeley, California

DISCLAIMER

This document was prepared as an account of work sponsored by the United States Government. While this document is believed to contain correct information, neither the United States Government nor any agency thereof, nor the Regents of the University of California, nor any of their employees, makes any warranty, express or implied, or assumes any legal responsibility for the accuracy, completeness, or usefulness of any information, apparatus, product, or process disclosed, or represents that its use would not infringe privately owned rights. Reference herein to any specific commercial product, process, or service by its trade name, trademark, manufacturer, or otherwise, does not necessarily constitute or imply its endorsement, recommendation, or favoring by the United States Government or any agency thereof, or the Regents of the University of California. The views and opinions of authors expressed herein do not necessarily state or reflect those of the United States Government or any agency thereof or the Regents of the University of California.

UCRL-11149
UC-34 Physics
TID-4500 (24th Ed.)

Research and Development

UNIVERSITY OF CALIFORNIA

Lawrence Radiation Laboratory

Berkeley, California

AEC Contract No. W-7405-eng-48

SCATTERING OF 250-MeV POSITIVE PI MESONS FROM A POLARIZED PROTON TARGET

Claude Henry Schultz

Ph.D. Thesis

January 17, 1964

Reproduced by the
Technical Information Division
directly from author's copy

Printed in USA. Price $2.25. Available from the
Office of Technical Services
U. S. Department of Commerce
Washington 25, D.C.

SCATTERING OF 250-MeV POSITIVE PI MESONS FROM A POLARIZED PROTON TARGET

Contents

Abstract v

I. Introduction 1

II. The Polarized Target

A. Dynamic Nuclear Orientation. 3

B. Apparatus. 11

1. Target Crystals. 11

2. Magnet 16

3. Cryostat 18

4. Microwave System 24

C. Detection, Measurement, and Calculation of the Target Polarization. 30

1. General Considerations 30

2. Q-Meter Detection. 31

3. Measurement Apparatus. 31

4. Calculation of the Polarization. 35

5. Measurement Procedure. 46

6. Polarization Results 52

D. Recent Improvements in the Polarized Target. 53

III. Elastic Pion-Nucleon Scattering. 60

IV. The Scattering Experiment

A. General Considerations 66

B. Pion Beam. 67

Contents (continued)

C. Counters and Electronics 74

D. Logic. 77

E. Normalization of Counting Rates. 80

F. Experimental Procedures. 80

1. Beam Monitoring. 80

2. General Procedures 82

3. Procedures at Individual Angles. 83

4. Asymmetry Measurements 85

5. Background 86

V. Calculations

A. Background Subtraction 88

B. Calculation of the Polarization. 89

1. Formulae and General Procedures. 89

2. Sample Calculation 91

C. Calculation of the Scattering Angles 95

VI. Results and Errors 98

VII. Discussion of Results. 102

Acknowledgments. 105

Appendix 107

References 112

SCATTERING OF 250-MeV POSITIVE PI MESONS FROM A POLARIZED PROTON TARGET

Claude Henry Schultz

Lawrence Radiation Laboratory
University of California
Berkeley, California

January 17, 1964

ABSTRACT

The polarization parameter in elastic π^+-p scattering has been measured at seven angles at a nominal incident meson kinetic energy of 250 MeV, by measuring the asymmetry in scattering from a polarized proton target. The data agree qualitatively with data obtained at 310 MeV by the double-scattering technique.

The polarized proton target consists of a 1-in.-cube volume of $La_2Mg_3(NO_3)_{12}\cdot 24H_2O$, in which the free protons in the water molecules, comprising 3% of the target by weight, are polarized. The average target polarization during the experiment was 20%, but has since been raised to more than 60%. A description is given of the target design and operation, and formulae are developed for calculating the average target polarization from the output of a nuclear magnetic resonance detector.

I. INTRODUCTION

The study of the low-energy pion-nucleon interaction has for many years been the subject of intensive experimental and theoretical work. The pion is believed to be the agent of the longest-range part of nuclear forces, the part most accessible to both experiment and calculation; it is also thought to be of great importance in the whole realm of the strong interactions.

A great many experiments have measured the differential and total cross sections of the $\pi^{\pm}$-p reactions at all accessible energies. In the last few years, the achievement of high-intensity pion beams has made possible the measurement of the recoil-proton polarization, which gives valuable independent information of the pion-nucleon interaction.

The most complete set of experiments to date has been carried out at 310 MeV pion kinetic energy.[1,2,3] Total and differential cross sections and recoil polarizations in π^{+}-p and π^{-}-p elastic scattering, as well as the differential cross section in π^{-}-p charge-exchange scattering, were used in an analysis intended to provide an unambiguous description of the scattering process in terms of the partial-wave amplitudes. The program did not achieve its goal, as no single unambiguous solution could be found. Although there was reasonable hope for success when the analysis was confined to s, p, and d waves (and higher partial waves were assumed not to contribute), the situation was much worse when nonzero f waves were allowed. A recent measurement by Hill and collaborators of the recoil-neutron polarization in π^{-}-p charge-exchange scattering offers some hope of removing the ambiguities.[4]

It appears desirable to undertake a similar program at a somewhat lower energy, at which the d-wave amplitude is small and the f-wave amplitude

might reasonably be expected to be zero. This experiment is part of such a program at 250 MeV.

For technical reasons it was desirable, and practically necessary, to measure the "polarization parameter," previously calculated from the recoil-proton polarization, by scattering from a polarized proton target. Already at 310 MeV the angular region in which the recoil-proton polarization could be measured was severely restricted by the small recoil energies; at 250 MeV the problem is much worse. With scattering from a polarized target, a second scattering to analyze the recoil-proton polarization is not needed. It is not absolutely necessary even to detect the recoil proton. The recoil-energy cutoff is thereby considerably lowered, making measurements at 250 MeV possible.

A polarized proton target has, of course, many potential uses in elementary particle physics. A large number of important experiments, either very difficult or downright impossible with other presently known techniques, become accessible with the availability of a polarized target. For this reason, the target has been designed and constructed so as to make it suitable for a wide variety of high-energy scattering experiments. Polarized proton targets have been previously constructed for low-energy physics.[5,6] To the author's knowledge the target described in this dissertation is the first polarized target suitable for high-energy experiments, and the π^+-p experiment is the first high-energy experiment performed with a polarized target. ("High energy" is intended to cover the region above 100 MeV kinetic energy in the laboratory frame of reference.)

II. THE POLARIZED PROTON TARGET

Because of the relatively weak fluxes available from existing particle accelerators in the energy region of several hundred MeV and above, and because of the relatively small cross sections, a useful polarized target should be as large as typical particle beams (several centimeters), with a hydrogen thickness comparable to that of typical liquid hydrogen targets (several tenths g/cm^2), and with a polarization at least as great as the statistical accuracies of most high-energy experiments (5 to 10%).

The target described in this report satisfies all the above criteria. The technique of dynamic nuclear orientation is used to obtain polarizations well over the minimum quoted above. The target is roughly a 1-in. cube of the rare-earth salt lanthanum magnesium nitrate ($La_2Mg_3(NO_3)_{12} \cdot 24H_2O$), in which the hydrogen nuclei in the waters of hydration are polarized. The hydrogen content is 3% by weight, and the hydrogen thickness is 0.15 g/cm^2. During the experiment the average polarization was 20%. It has since been raised to more than 60%.

A. Dynamic Nuclear Orientation

The effects and techniques known collectively as dynamic nuclear orientation are based on the idea of a forced redistribution of the populations of the magnetic quantum levels of a system containing two or more kinds of spins. Typically one of the spins has a large magnetic moment (comparable to that of a free electron), and is highly polarized in a strong external magnetic field at low temperature. The other kind of spin has a small magnetic moment and is only minutely polarized in thermal equilibrium at available temperatures. Transitions induced in the system have the effect of transferring

the high polarization to the spins with the low magnetic moment. The natural polarization of these spins is thus "dynamically enhanced."

The many forms of dynamic nuclear orientation have been extensively studied theoretically and experimentally by various authors.[7] Only those concepts pertinent to the target used in this experiment are discussed here.

The target consists of four single crystals of lanthanum magnesium nitrate, in which a small fraction of the lanthanum ions is replaced by Nd^{142}. The La ions are diamagnetic, but the Nd ions are paramagnetic, owing to the presence of three 4f unpaired electrons in an inner shell. The resulting crystal is a dilute paramagnetic substance, in which the paramagnetic centers are sufficiently far apart so that their spin-spin interaction may be neglected.

Although the ground state of the free Nd^{+++} ion is $I_{9/2}$, the presence of the crystalline electric fields causes a partial splitting of the states with different orbital angular momentum quantum number, resulting in a splitting of the $2J + 1 = 10$ substates into five "Kramers doublets" each of which is further split by the applied magnetic field. The splitting, in units of temperature, between the two lowest doublets is $47.6^{\circ}K$, so that near $1^{\circ}K$ only the lowest doublet is appreciably populated, and has the effective spin value $S = 1/2$. The spin system is described by an effective spin Hamiltonian in which the paramagnetic neodymium ions act like free unpaired electrons with effective spin 1/2, and with a magnetic moment of the same order of magnitude as that of free electrons. To conform with general usage, and for brevity, these will henceforth be called electron spins.

Consider now a simplified system consisting of one electron spin and

one proton spin, in a strong external magnetic field at liquid helium temperature. The energy-level diagram is shown in Fig. 1. The large splitting, Δ, corresponds to the two possible orientations of the electron spin with respect to the magnetic field; the small splitting, δ, to the two orientations of the proton spin. Note that $\Delta/\delta \approx 10^3$. The quantum numbers of the four states are listed in Fig. 1. The heavy lines indicate the zero-order transitions $\Delta M = \pm 1$, $\Delta m = 0$ (M and m are the magnetic quantum numbers of the electron and proton spins respectively), i.e., the transitions involved in paramagnetic resonance and electron spin-lattice relaxation. The relative populations of the four energy levels at thermal equilibrium are listed in Fig. 1. The proton polarization, defined as

$$P_T = \frac{(\text{no. protons with } m = 1/2) - (\text{no. protons with } m = -1/2)}{\text{total no. protons}}, \quad \text{(II-1)}$$

is, by Boltzmann statistics, $\tanh(\delta/2kT)$. The electron polarization is $\tanh(\Delta/2kT)$.

In addition to the electronic and nuclear Zeeman terms giving rise to the four energy levels of Fig. 1, there is a weak dipole-dipole coupling between electron and proton spins which mixes the levels slightly and gives rise to partially forbidden transitions such as $\Delta M = 1$, $\Delta m = 1$ (the dotted line in Fig. 1). If one saturates this transition by applying microwave power of the proper frequency to the crystal, one can, to good approximation, equalize the populations of the two levels involved. Since the remaining two energy levels are linked to the two equally populated levels by the zero-order spin-lattice relaxation mechanism, the result is a redistribution of the steady-state populations as shown in the last column in Fig. 1. The proton polarization can now be calculated according to Eq.(II-1) to be

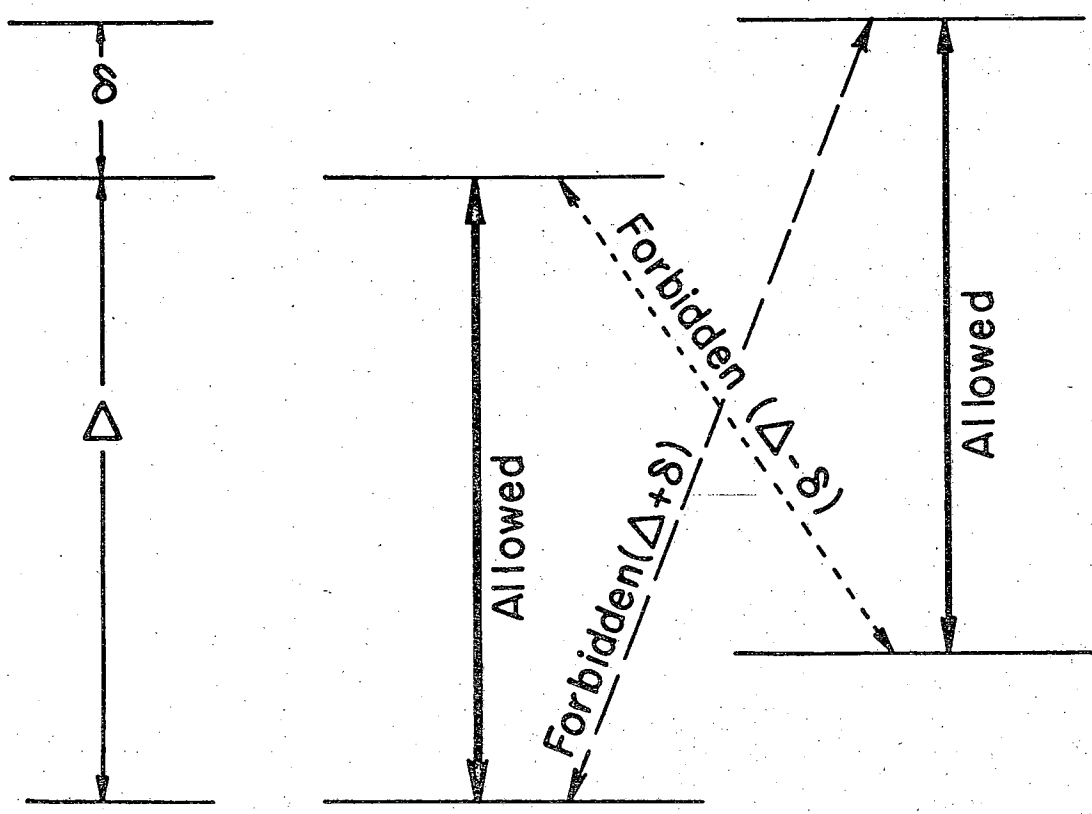

M	m	Relative population at thermal equilibrium	Relative population when saturating Δ - δ
$+\frac{1}{2}$	$-\frac{1}{2}$	$e^{-(\Delta+\delta)/kT}$	$e^{-\Delta/kT}$
$+\frac{1}{2}$	$+\frac{1}{2}$	$e^{-\Delta/kT}$	1
$-\frac{1}{2}$	$-\frac{1}{2}$	$e^{-\delta/kT}$	1
$-\frac{1}{2}$	$+\frac{1}{2}$	1	$e^{+\Delta/kT}$

Fig. 1. Energy levels of an electron and a proton spin in an external magnetic field, showing magnetic quantum numbers of the four states and relative populations at thermal equilibrium and when saturating the partially forbidden transition at frequency $(\Delta - \delta)/h$.

MU-32843

$\tanh(\Delta/2kT)$, equal to the original electron polarization. The proton thermal equilibrium polarization has been enhanced by a factor $\Delta/\delta \approx 10^3$.

If, instead, the other partially forbidden transition, $\Delta M = 1$, $\Delta m = -1$ (indicated in Fig. 1 by the dashed line) is saturated, the population levels are redistributed in such a way as to result in a proton polarization $-\tanh(\Delta/2kT)$. The minus sign indicates that this polarization is in the opposite direction to the thermal equilibrium polarization.

Both of the partially forbidden transitions that induce dynamic polarization involve the simultaneous flip of an electronic and nuclear spin. Thus, one can think of the mechanism of dynamic polarization as a transfer of polarization from the electron to the proton spins.

The above picture is, of course, far from a complete explanation. The crystals used for the polarized target contain several thousand free protons for every neodymium ion. However, the electron relaxation time is of the order of milliseconds, while that of the protons is about 10 minutes under typical conditions; thus, each electron spin can successively flip the several thousand proton spins as required, relaxing after each flip via spin-lattice relaxation, then coupling with another proton and repeating the process. These relaxation times are highly temperature-dependent, and this fact severely restricts the temperature range in which dynamic polarization can be successfully carried out. This leads to a further condition (in addition to saturating the forbidden transition)

$$T_{1e}/T_{1p} \ll N_e/N_p \,, \qquad \text{(II-2)}$$

where T_{1e} and T_{1p} are the electron and proton relaxation times, and N_e and N_p are the electron and proton densities.

The dipole-dipole interaction between electron and proton spins is highly distance-dependent (r^{-6}), and the electron spins can couple and undergo a mutual spin flip with only the small number of protons that are their nearest neighbors. The polarization of the protons then spreads outward from these "sources" through the volume of the crystal by means of the proton-proton dipole-dipole interaction, which causes mutual spin flips of neighboring protons. In this way the electron spins always have a fresh supply of neighboring proton spins waiting to be flipped. Since the proton-proton "flip-flop" transition conserves magnetic energy, it is highly allowed, and the polarization diffuses throughout the crystal in a few minutes. In other words, a weak proton-proton coupling suffices to cause interchange of spin states because the Larmor frequency of the two protons involved is substantially identical.

To summarize, the effective spin Hamiltonian for the composite electron-proton spin system can be written

$$\mathcal{H} = g\beta \sum_k \vec{H}_o \cdot \vec{S}_k + g_n \beta_n \sum_i \vec{H}_o \cdot \vec{I}_i + \sum_{i,k} D_{ik} + \sum_{i,j} U_{ij} , \qquad \text{(II-3)}$$

where the four terms represent, in turn, the electronic Zeeman, nuclear Zeeman, electron-proton dipole-dipole, and proton-proton dipole-dipole interactions; β and β_n are the Bohr and nuclear magnetons, g and g_n are the spectroscopic splitting factors for the "electron" and proton spins, H_0 is the external magnetic field, S_k is the spin of the $\underline{k}$ th electron, and I_i is the spin of the $\underline{i}$ th proton.

The allowed electron spin-flip transition occurs at $\nu_e = \Delta/h$, where $\Delta = g\beta H_0$. Dynamic proton polarizations of magnitude $\tanh(\Delta/2kT)$, either parallel or antiparallel to the direction of H_0, can be induced by saturating the partially forbidden transitions at $\nu_e \pm \nu_n$ (where $\nu_n = \delta/h = g_n\beta_n H_0/h$), in which an electron and a proton spin are simultaneously flipped. The proton polarization is a steady-state polarization and can be maintained as long as the proper forbidden transition is successfully saturated.

In practice, the full theoretical value of the proton polarization is never reached. Two reasons for this are:

(a) The resonance lines at ν_e and $\nu_e \pm \nu_n$ are not completely resolved. The widths of the resonance lines are typically ≈ 5 gauss, which is of the same order of magnitude as their separation $\Delta H = H_0\, g_n\beta_n/g\beta$, so that at the same time as one saturates the desired forbidden transition at $\nu_e \pm \nu_n$, one also induces electron spin flips due to the tail of the resonance centered at ν_e. This decreases the electron polarization at a given field and temperature, and consequently decreases the attainable proton polarization, since the theoretical upper limit of the proton polarization is the existing electron polarization.

(b) The theoretical proton polarization is based on the assumption that the protons do not relax toward thermal equilibrium. In practice, the proton relaxation time is noninfinite, owing partly to the presence of very small amounts of paramagnetic impurities other than neodymium, which provide a mechanism for the relaxation of the proton spins.

In conclusion, a brief description will be given of the experimental conditions necessary for successfully polarizing the protons in the target under discussion.

(a) The target must be in a strong external magnetic field. Since ν_n/ν_e is of the order of 10^{-3}, the resonance which polarizes and that which depolarizes differs by only 1 part in 1000 in frequency at a given field, or alternatively in magnetic field at a given frequency. The fractional amount by which the field may vary over the volume of the target should therefore be much smaller than 1 part in 1000. Similarly, the magnitude of the field should be constant in time (free from drifts, ripple, and random fluctuations) to the same accuracy as it is uniform in space. Within these limitations, the field should be as strong as possible, in order to maximize the electron polarization. Also, since the widths of the resonance lines are very roughly independent of field, a stronger field results in better resolution of the desired resonance line and consequently in less depolarization.

(b) The target must be in good thermal contact with a cold bath. Within the limitations imposed by the proton and electron relaxation times, the target should be as cold as possible, again in order to maximize the electron polarization. An approximate upper limit is the temperature of liquid helium at 1 atmosphere (4.2°K); above this temperature the electron relaxation time becomes so short that it is difficult to saturate the forbidden transitions. Ideally the proton polarization should increase as the temperature decreases, although at sufficiently low temperatures the inequality (II-2) may break down because of a different temperature

dependence of T_{1e} and T_{1p}, due to, say, impurities.

(c) The target must be exposed to microwave radiation of the right frequency and of sufficient intensity to saturate one of the polarizing resonances. The radiation must be monochromatic and constant in frequency to within the same fractional tolerances as those on the uniformity and time stability of the magnetic field, for the same reason.

The apparatus used to realize these experimental conditions is described in the following sections.

B. Apparatus

1. The Target Crystals

Lanthanum magnesium nitrate is a crystal with threefold axial symmetry. The spectroscopic splitting factor of neodymium ions imbedded in lanthanum sites is strongly direction-dependent, varying from 0.36 when the line of axial symmetry is parallel to the external field to 2.70 when it is perpendicular. (By this definition the spectroscopic splitting factor of a free Dirac particle with the mass of the electron is 2.) In order to have the same fine-structure splitting in a given field for all neodymium ions, single crystals of lanthanum magnesium nitrate are used. Furthermore, all four single crystals are stacked together with their line of axial symmetry perpendicular to the field, so that g is maximum, the fractional variation of g with angle of orientation is minimum, and hence any small misalignments among the crystals have minimum effect. (It may, in principle, be possible to obtain somewhat higher polarization by rotating the crystals away from this orientation, because for a given microwave frequency the field would be higher and consequently the desired resonance would be better resolved. This

was attempted, at 30° and 45° from the perpendicular orientation, but the crystals could not be lined up well enough with respect to one another to give a single resonance line.)

The single crystals are grown from a saturated solution of $La_2Mg_3(NO_3)_{12} \cdot 24H_2O$ in which 1% of the La ions is replaced by nearly 100% enriched Nd^{142}, which has no hyperfine structure, so that the energy-level diagram of Fig. 1 is valid. They are grown in a desiccated atmosphere in a temperature bath at $0^{\circ}C$. Figure 2 shows the apparatus used to grow the crystals. First, a solution of lanthanum magnesium nitrate is made up by mixing the proper amounts of lanthanum nitrate and magnesium nitrate, adding enough water to bring the solution below the saturation level at $0^{\circ}C$. Then the solution is doped with the proper amount of neodymium nitrate, made by mixing neodymium oxide, nitric acid, and water.

The solution is then brought nearly to saturation by heating it to drive off the excess water. It is placed in a flat glass dish inside a desiccator, and the desiccator is placed in an ice bath. In a few days a great many small crystals begin to form on the bottom of the dish. As soon as they are large enough so that their shape can be determined by the naked eye, they are removed from the dish, and those which have the most perfect hexagonal shapes are kept as "seeds" from which to grow large crystals, while the rest are re-dissolved.

The good seeds are placed in individual dishes, each on a small pedestal in the bottom of a dish, so that they are able to grow freely in all directions. The crystals continue to grow in approximately hexagonal shape until, in about 2 weeks, they are 1/4 in. thick and about 1 in. across.

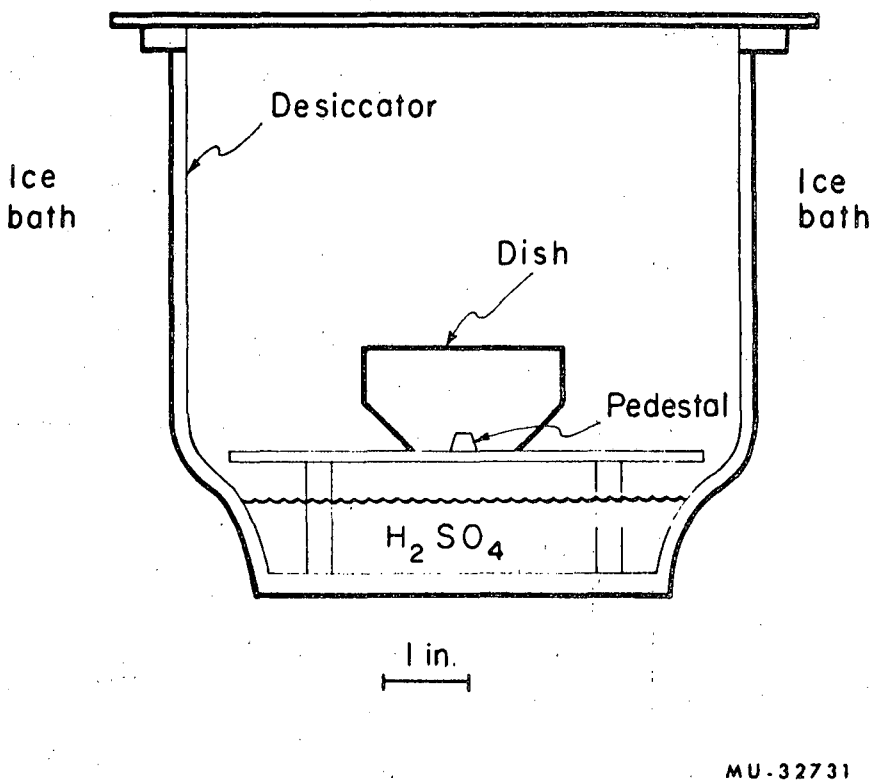

Fig. 2. Desiccator and dish in which the crystals of lanthanum magnesium nitrate are grown.

Figure 3 shows some crystals grown in this way. Four such crystals are stacked together to make the target volume a 1-in. cube. When necessary, the crystals are cut to the size of their container (see Sec. VI.B.4) with a moist string saw. Good single crystals are clear and nearly transparent, with no internal cracks or discontinuities.

The Nd ions appear not to crystallize as readily as the La ions, and it is estimated that crystals grown from a 1% doped solution contain only about 0.2% Nd.[8] However, as crystals are grown until a sizeable fraction of a particular batch of solution has crystallized, the remaining solution is more heavily doped than at the beginning, so that the crystals are also more heavily doped. This was the case with the crystals used in this scattering experiment: the four crystals were grown successively from the same batch of 1% doped solution. The fraction of Nd ions in each crystal, or the average for all four crystals, is not known; it is believed to be smaller than, but of the order of magnitude of, 1%. The optimum proton polarization obtainable appears to be roughly independent of doping in this region.[9]

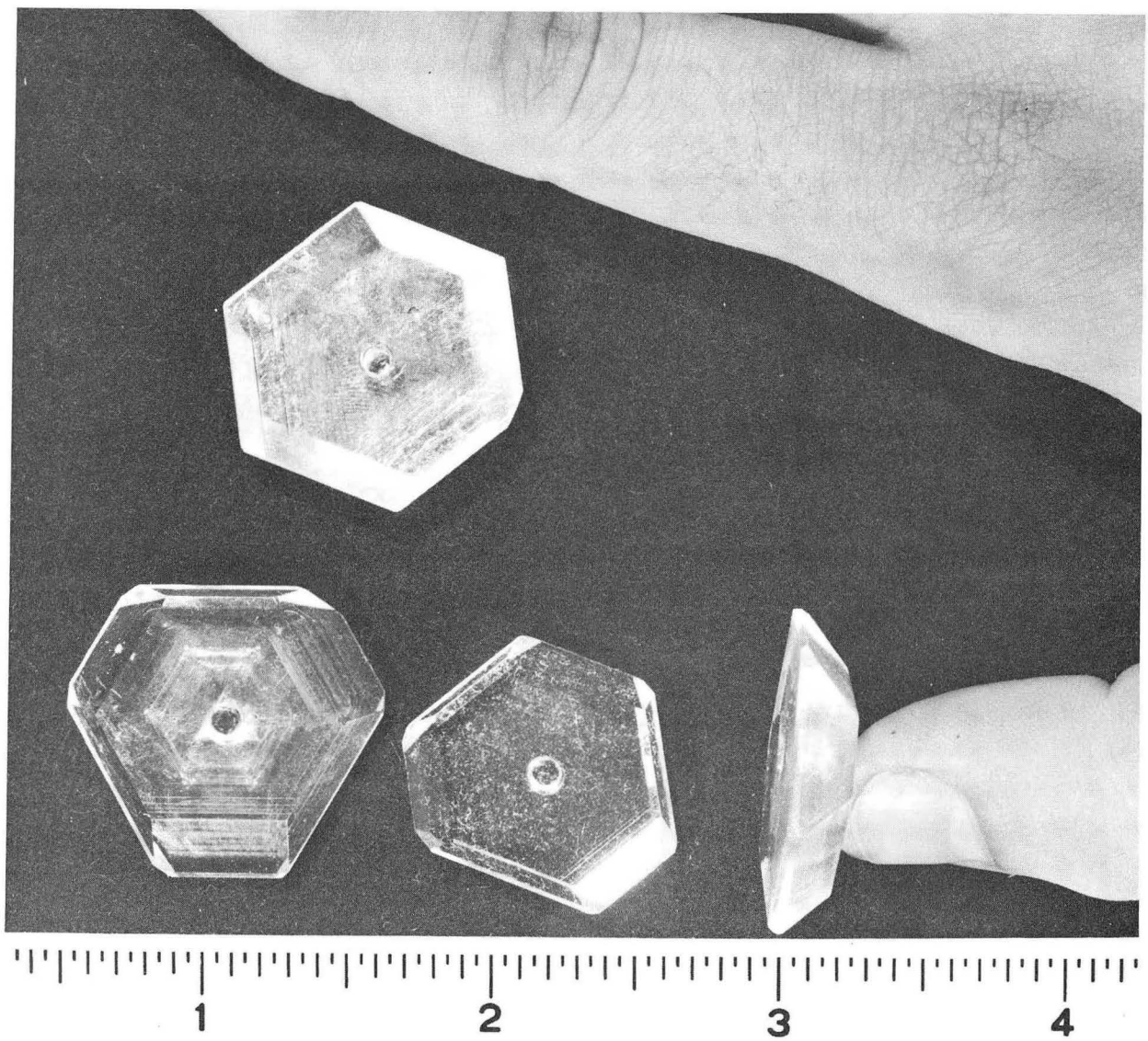

ZN-4154

Fig. 3. Photograph of some crystals of lanthanum magnesium nitrate. The crystals grow in all directions, including downward, from the starting position on the pedestal; hence the holes in the middle. Scale is in inches.

2. Magnet

The magnet used for polarizing the electron spins is an iron-core electromagnet pictured schematically in Fig. 4. The magnet, named "Pia," is an H magnet with a 4-in. gap, and with circular pole pieces of 18-in. diameter at the gap, flaring out at a 45° angle to 26 in. at the base. The flaring of the pole pieces is to lessen the effects of magnetic saturation in the pole pieces. This saturation begins and is most severe at the edge of a square-cut pole piece. Flaring the edge of the pole piece decreases the flux density near the edge in the gap, enabling the iron in this region to carry fewer flux lines. The success of this method of lessening magnet saturation is evidenced by the fact that the magnetization curve is a straight line up to 16 000 gauss. By preventing saturation of the poles, a more uniform field is achieved at the center of the magnet, for a given pole diameter. The need for field uniformity is discussed in Sec. II.A.

The energizing current is carried in 0.467-in.-square copper conductor with a 0.275-in.-diameter center hole for water cooling. The conductor is wound into two coils of 66 turns each, placed around the pole pieces as shown in Fig. 4. The nonrectangular cross section of the coils was dictated by the desire to get as much current as possible as close as possible to the magnet center.

The magnet is designed for a maximum current of 2000 A, at which current the central field is 24 000 gauss. At a central field of 9100 gauss (at which the magnet was used during the scattering experiment), the variation from the central field in a 1-in. cube at the center of the gap is 1 part in

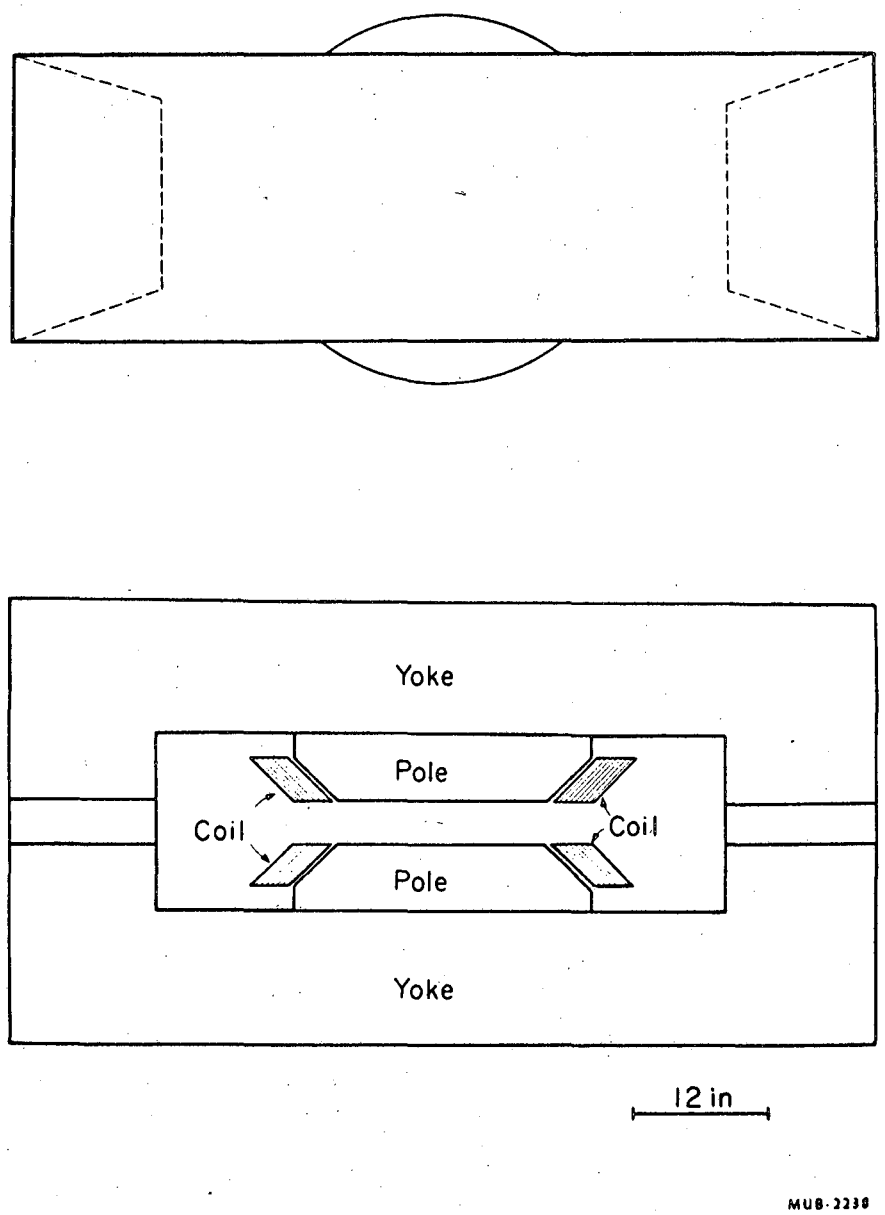

Fig. 4. Scale drawing of two views of the magnet Pia.

70 000. At a central field of 18 800 gauss, at which the magnet has been used more recently (see Sec. II.D), this variation is 1 part in 20 000. The overall dimensions of the magnet are 76 x 36 x 26 in., and its weight is 18 500 lb.

The current is supplied by a three-phase full-wave solid-state power supply with LC filtering. Current regulation is achieved with an induction voltage regulator designed by Ivan Lutz and Robert Sorensen of this Laboratory. It is capable of regulating currents up to 1700 A, with short-term (≈ seconds) regulation of 1 part in 50 000, and long-term (≈ hours) regulation of 1 part in 10 000.

3. Cryostat

The cooling of the target crystals is achieved by immersing them in a bath of liquid helium. The helium is maintained at a vapor pressure of about 1 mm Hg by continuous pumping, making the temperature of the bath about 1.2°K.

A schematic diagram of the helium cryostat is shown in Fig. 5. The helium vessel consists of a 10-in.-diam 12-in.-long reservoir, with a 2-in.-diam lower extension that reaches into the magnet gap. Attached to this extension is a 2-in.-diam 11-in.-long flask, made of thin foil to minimize the amount of extraneous material in the path of the particle beam. During the experiment, the flask was 0.005-in. Mylar, but it has since been replaced by 0.003-in. aluminum alloy (see Sec. II.D). The target is inside the flask, near the bottom.

Above the liquid helium reservoir is a 3-ft-long neck of 1/64-in. stainless steel, made long and thin to minimize the heat conduction to the

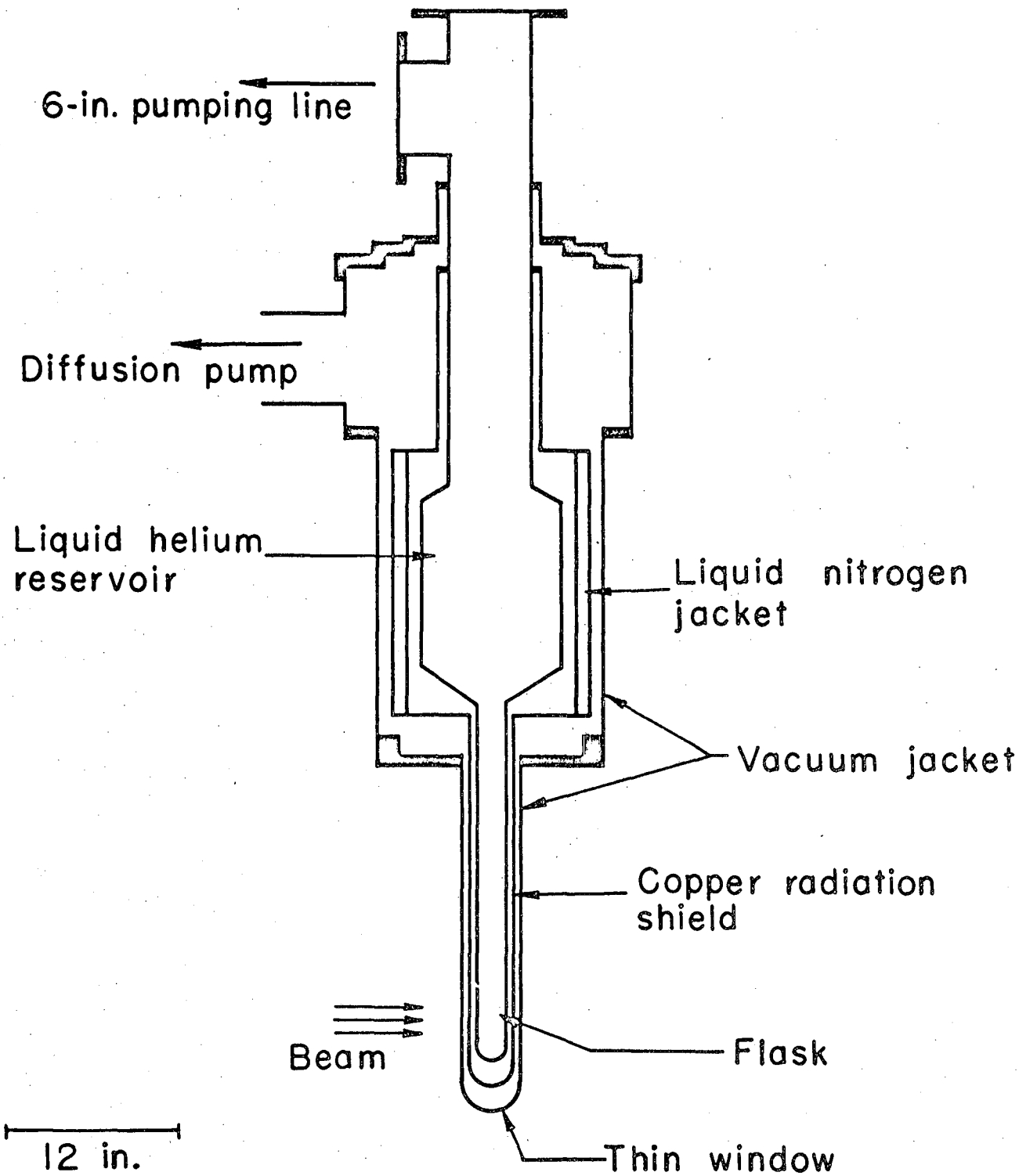

MU-28654A

Fig. 5. The cryostat used for cooling the target crystals.

reservoir.

The reservoir is surrounded by an insulating vacuum jacket, whose pressure is kept at approximately 10^{-6} mm Hg by an oil diffusion pump. The outer container is made of stainless steel; its lower extension, which fits inside the magnet gap, is of rectangular cross section, with a rounded bottom, around which is fastened a thin "wrap-around" window, through which the beam and scattered particles enter and leave. During the experiment this window was of 0.005-in. Mylar, but it also has been replaced with 0.003-in. aluminum alloy.

A hollow cylindrical liquid nitrogen radiation shield surrounds the helium reservoir. From this shield a copper extension, in good thermal contact with the liquid nitrogen, reaches up to make thermal contact at a point high on the neck of the helium reservoir, in order to decrease the temperature gradient up the neck, and therefore the heat input by conduction to the helium reservoir. Another copper extension surrounds the 2-in.-diam helium flask, except in the region where the material is to be kept at a minimum because of the scattering experiment. This acts as a radiation shield around the flask. The sides of the copper shield that are perpendicular to the magnetic field are slotted, to prevent damage to the cryostat due to eddy currents when the magnet is accidentally turned off. This also allows a modulation field at 400 cps to be applied (see Sec. II.C.3).

The outside of the helium container and the outside of the radiation shield, along the entire length of the cryostat, are each wrapped with several layers of 0.00025-in. aluminized Mylar for additional radiation shielding.

A scale drawing of the bottom part of the cryostat, including the magnet pole faces and the target, is shown in Fig. 6. The target is suspended from the cover plate at the top of the cryostat by the waveguide through which the target is irradiated with microwave power (see Sec. II.B.4). Bronze waveguide is used, with the walls thinned down to 0.015 in. Four steel baffles are attached to the waveguide in the region where it passes through the neck of the helium vessel, concentric with and of slightly smaller diameter than the neck. These act as radiation shields between the cover plate and the helium reservoir. In addition, being cooled by the helium vapor, they cool the waveguide and thereby decrease the temperature gradient down the waveguide. This reduces the not negligible heat input to the liquid helium by conduction down the waveguide, and utilizes the considerable cooling power of the helium vapor. The baffles also force the helium vapor to rise through the neck close to the wall, so that the heat exchange cools the metal of the neck. Figure 7 is a photograph of the waveguide, target container, baffles, etc.

The total heat input to the liquid helium by radiation and conduction is about 1/3 watt, causing a boiloff rate of 1/3 liter of liquid helium per hour.

The helium system is pumped out through a 6-in.-diam opening near the top of the cryostat (see Fig. 5). The pump is a 15-hp mechanical pump with a capacity of 310 ft^3/min. It keeps the helium at a vapor pressure of about 1 mm Hg, corresponding to a temperature of 1.2°K.

Three 100-Ω 1/4-W carbon resistors placed at different levels in the cryostat are used to monitor the liquid helium level. Their resistances are

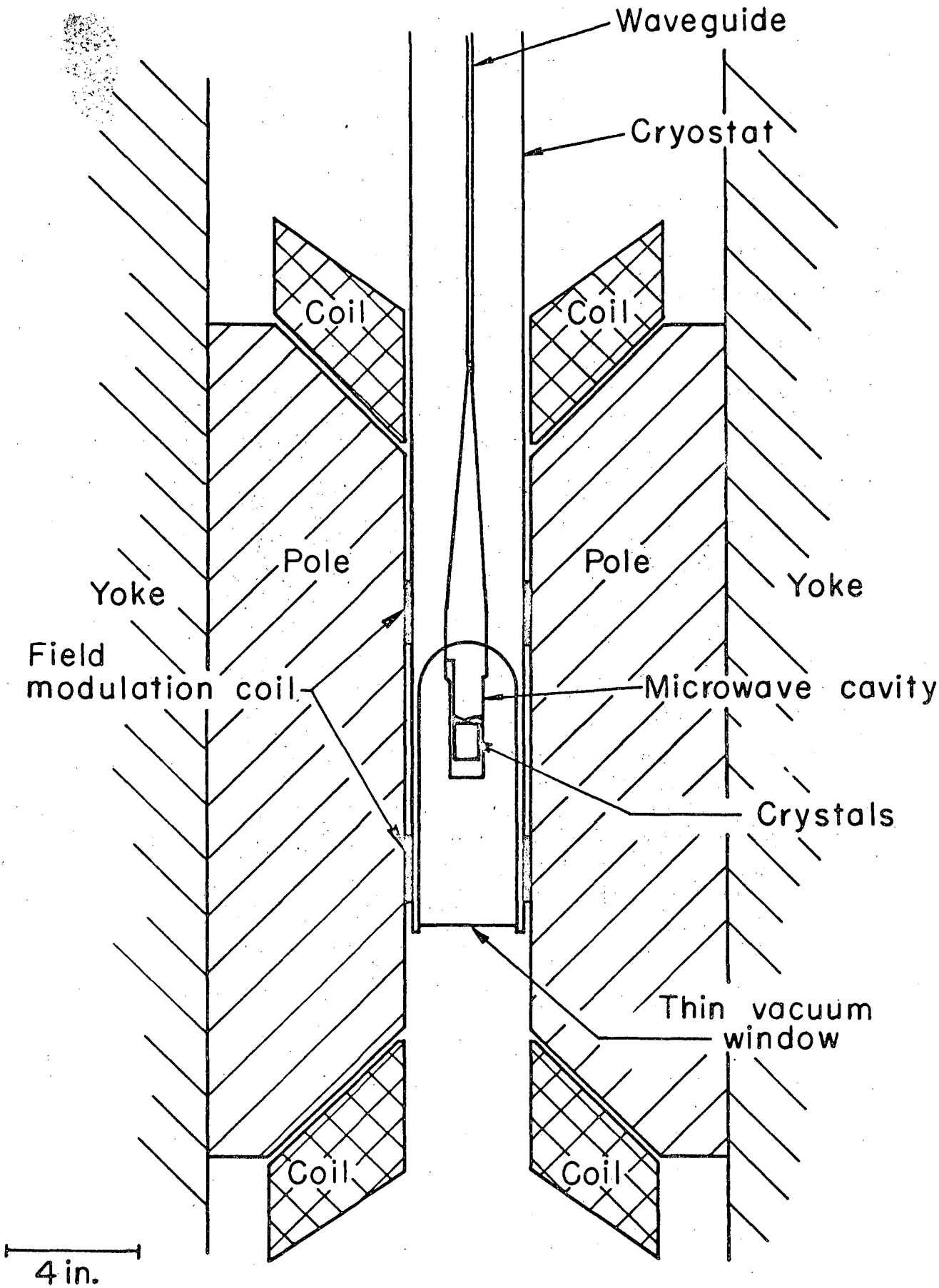

MU-28649A

Fig. 6. Detailed view, looking down the beam line, of the polarized target apparatus.

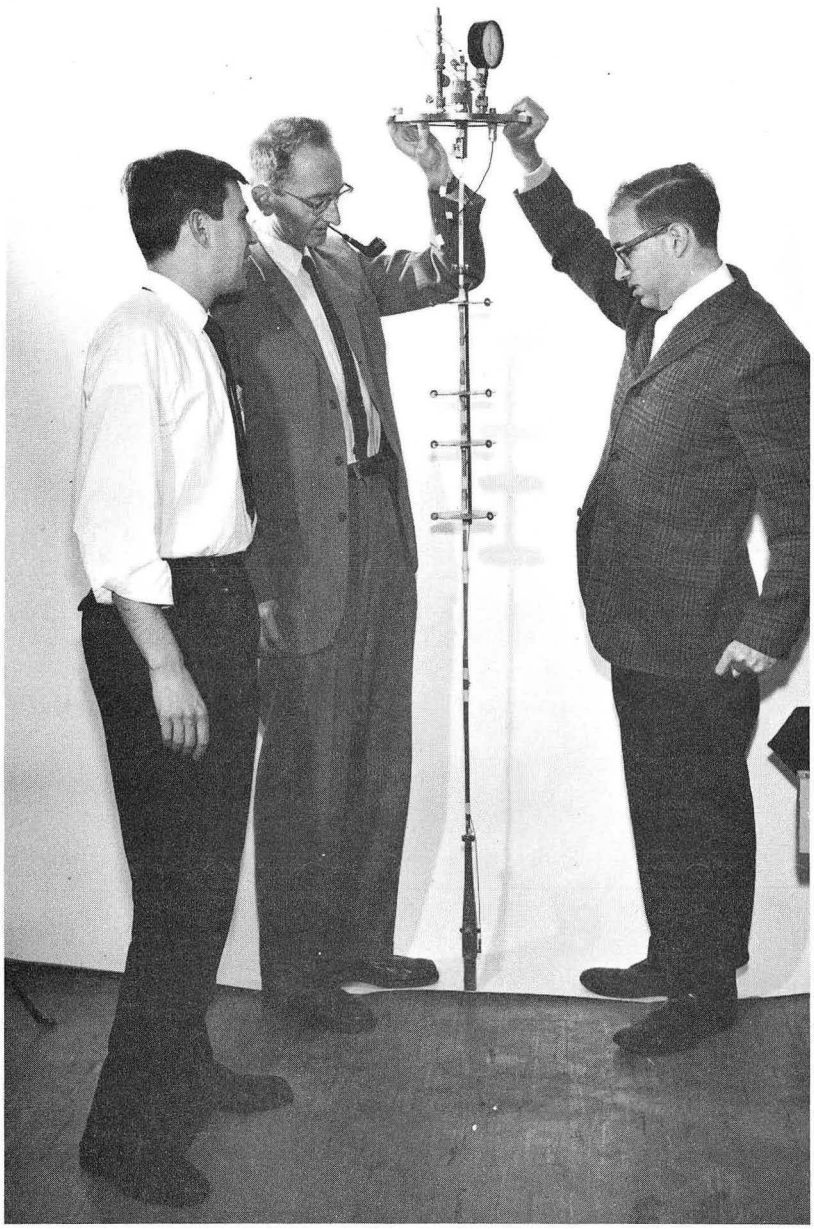

ZN-4156

Fig. 7. The author, Professor Owen Chamberlain, and Professor Gilbert Shapiro with the target container (at the bottom) suspended by 5 ft of waveguide from the liquid helium reservoir cover flange. Note the baffles on the waveguide, intended to better utilize the cooling power of the helium boil-off gas, and the thin coaxial cable which connects the target with the Q-meter polarization detector (see Sec. II. C. 2) outside the cryostat.

measured by a bridge circuit in which the voltage is supplied by a 22.5-V dry cell battery and the two fixed legs of the bridge circuit are 10 000 Ω each. When immersed in liquid helium at atmospheric pressure, the nominally 100-Ω resistors rise to about 600 Ω, while at 1.2°K they are about 700 Ω.

The relative positions and orientations of magnet and cryostat are shown schematically in Fig. 8. The unusual orientation of the magnet is convenient because it simultaneously enables the beam to enter the gap horizontally and the cryostat to enter vertically without interference from the magnet yoke or pole pieces.

4. Microwave System

A schematic diagram of the signal generator and associated equipment used in saturating the partially forbidden spin transitions is shown in Fig. 9.

The signal generators used during the experiment were floating-drift-tube klystrons operating at about 34 kMc/sec, with a power output of several watts, manufactured by Elliott Brothers, Ltd.

The target crystals are contained in an untuned cavity connected to the microwave tube by about 8 ft of waveguide. The dimensions of the cavity are 1 x 1 x 5.5 in. The transition from the 0.280 x 0.140-in. (8-mm) waveguide to the 1 x 1-in. cavity is made by an 8-in.long, gradually flaring horn, in order to decrease the amount of microwave power reflected at the entrance to the cavity. A photograph of cavity and horn is shown in Fig. 10.

The crystals fill up a 1-in.^{3} space near the end of the cavity. The last 3-1/4 in. of the cavity is constructed of 0.002-in. copper, to minimize particle scattering by the cavity. The rest of the cavity and the horn are made of 1/8-in. copper. Figure 11 is a cutaway drawing of the cavity.

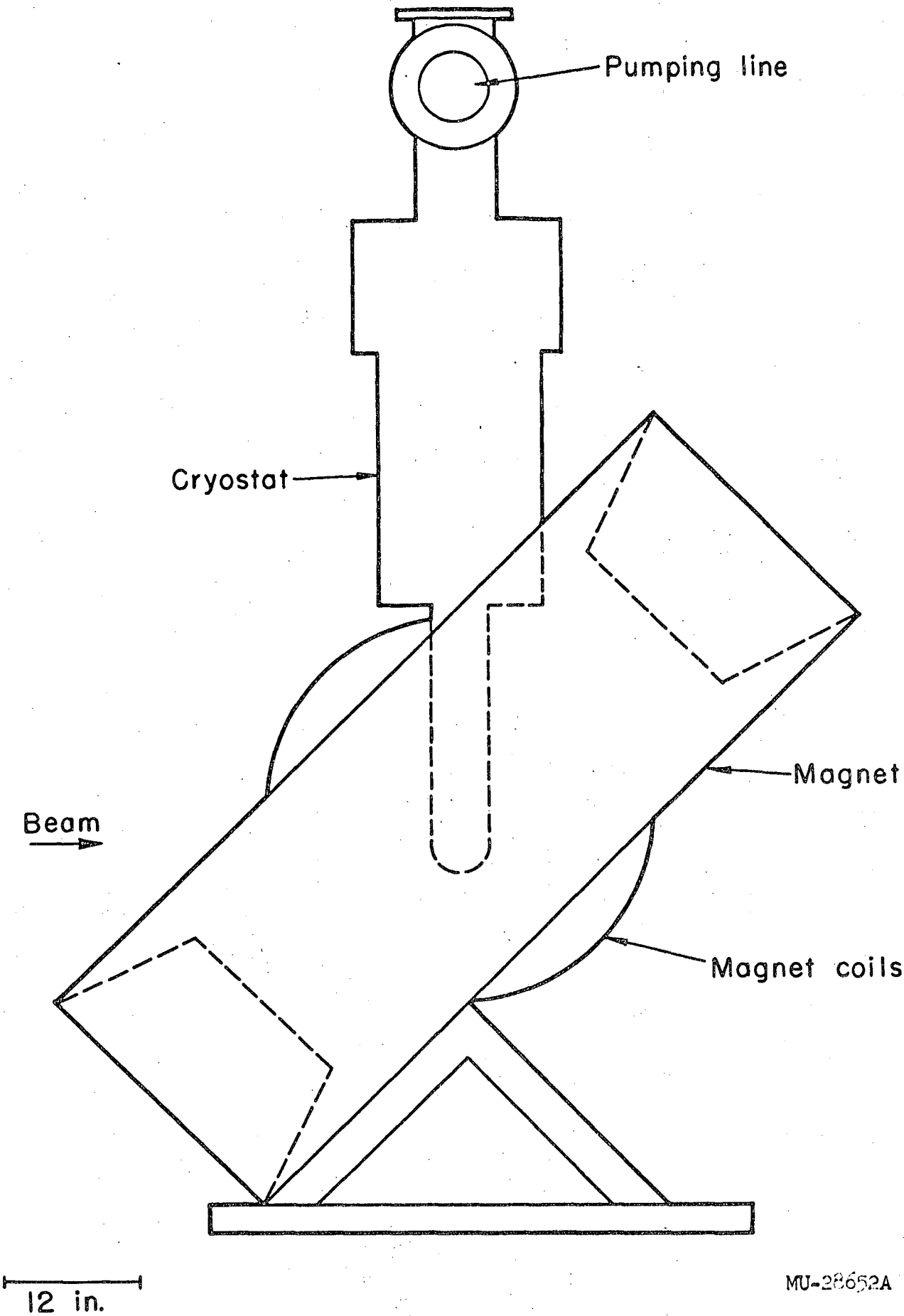

Fig. 8. The relative positions and orientations of the magnet and cryostat. The target is at the center of the magnet.

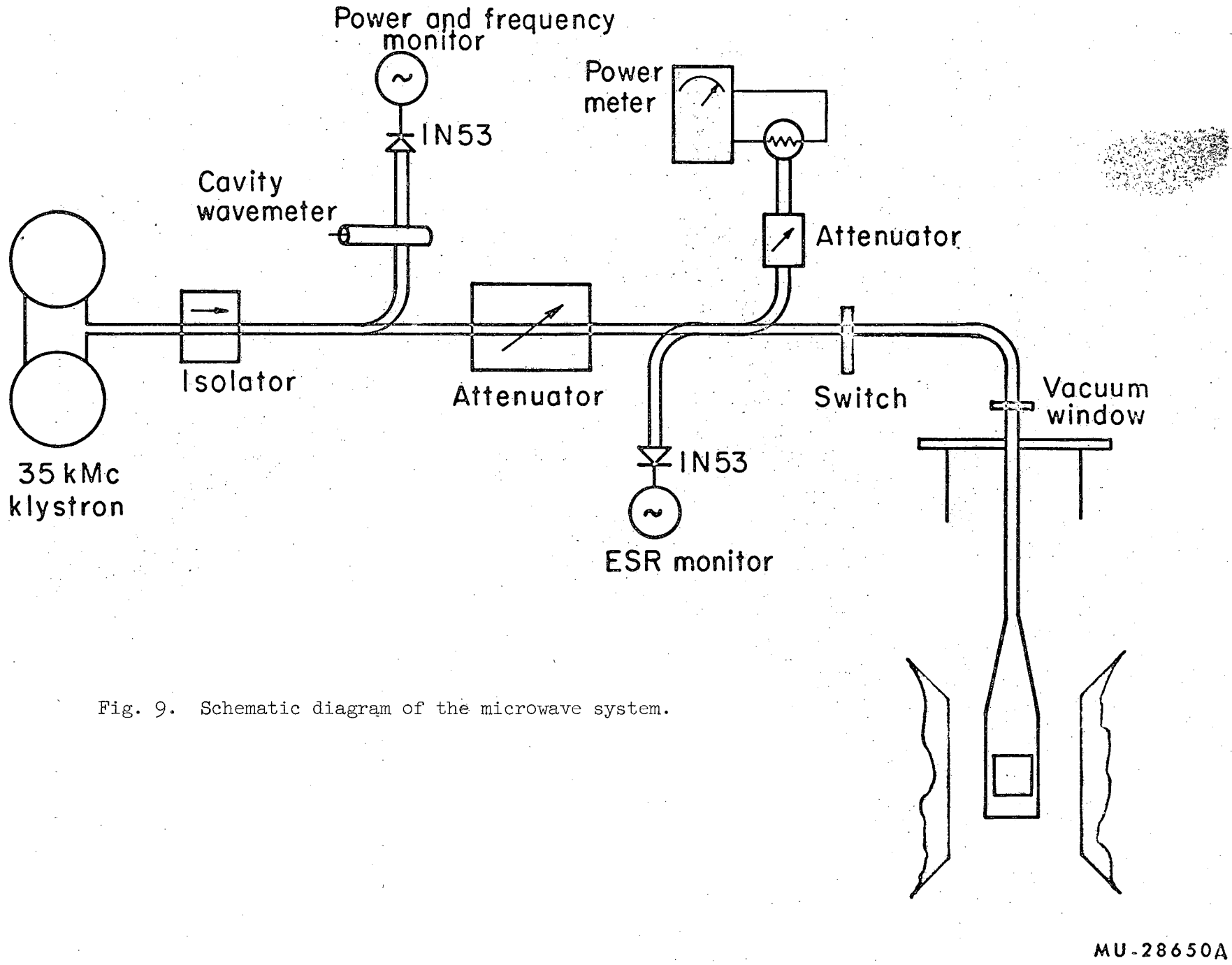

Fig. 9. Schematic diagram of the microwave system.

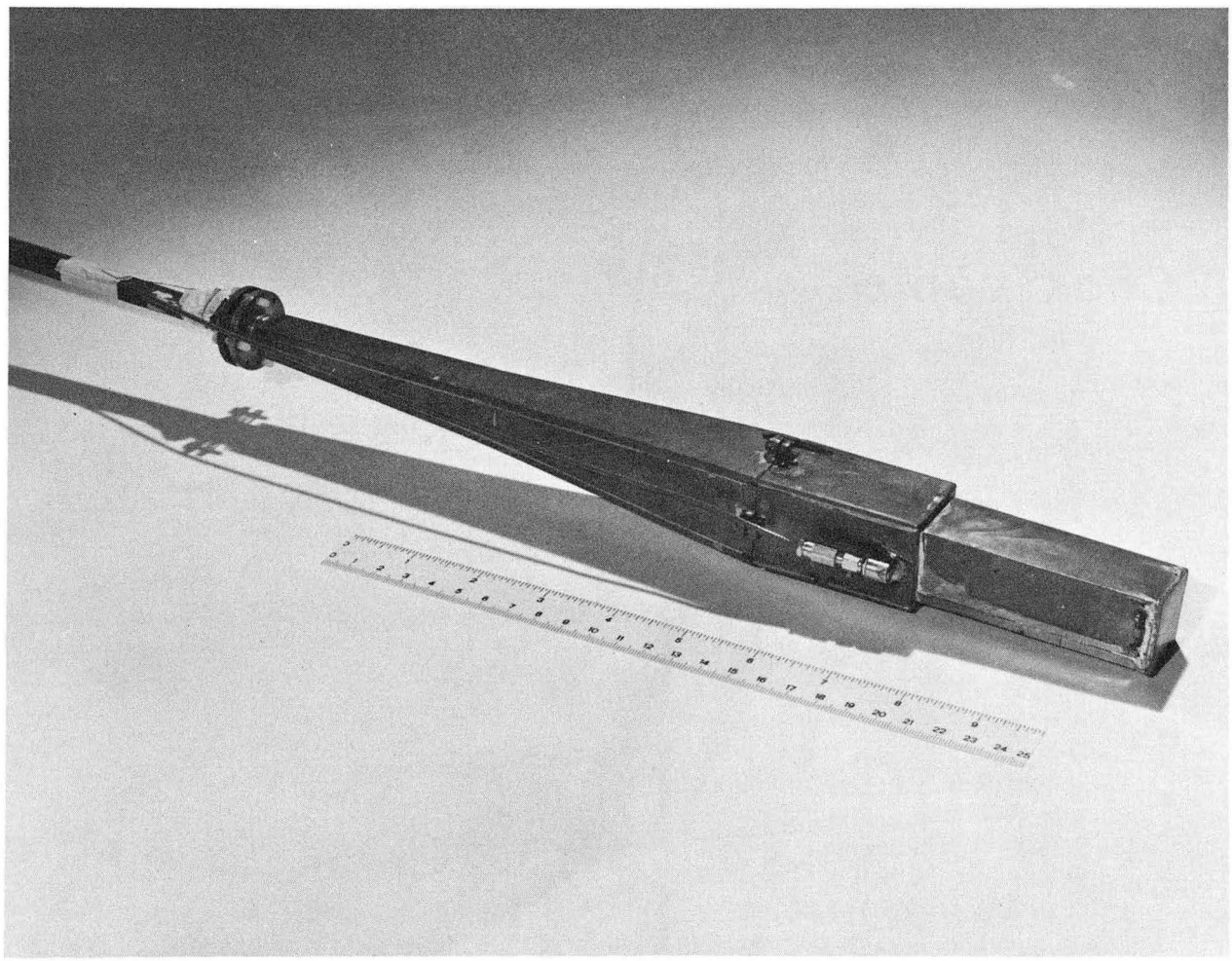

ZN-4155

Fig. 10. Photograph of the microwave cavity and transition piece. Also shown is the coaxial cable used in the detection of the target polarization (see Sec. II. C. 2).

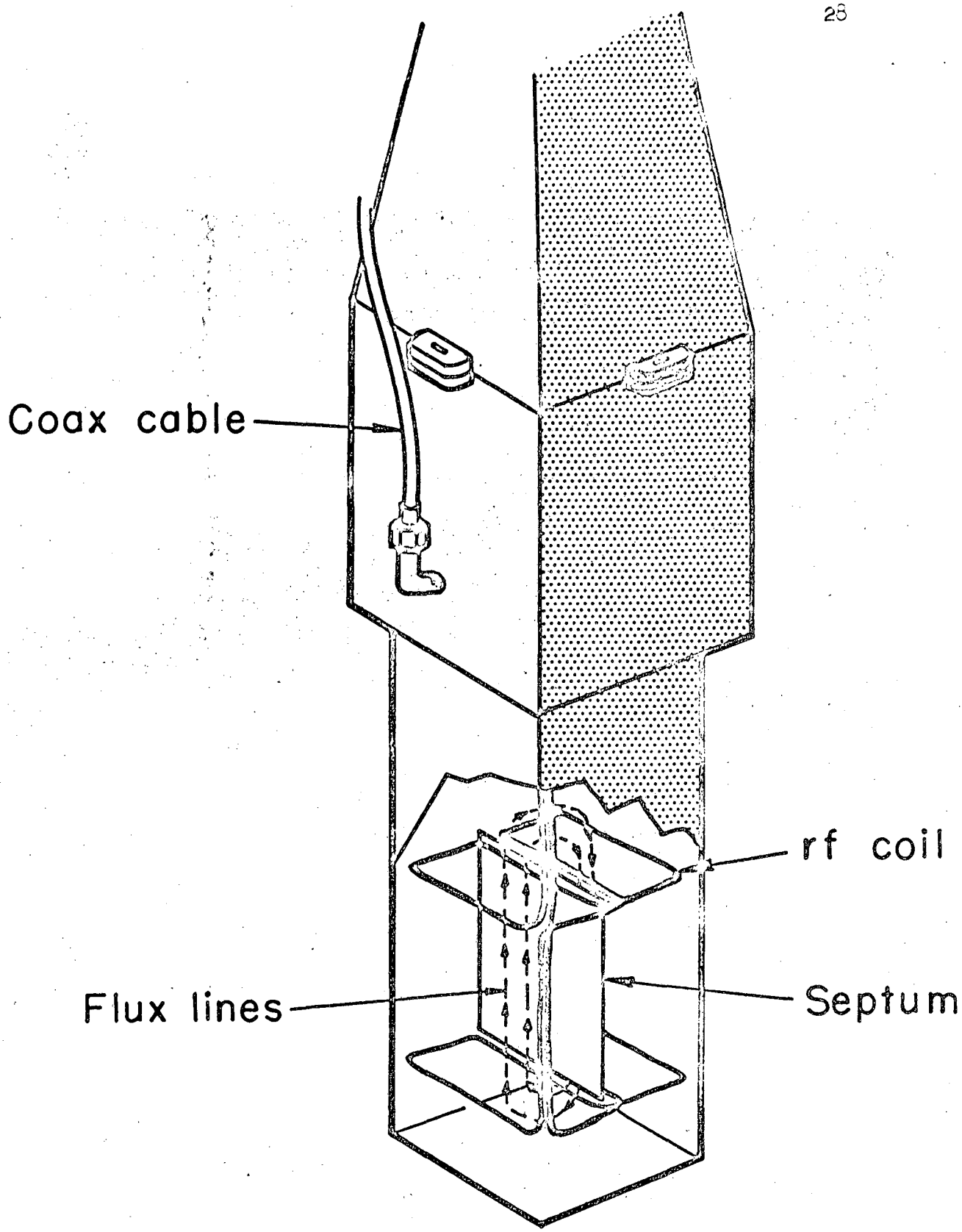

Fig. 11. Cutaway drawing of the microwave cavity and NMR pickup coil.

MU-28653

It is estimated that the cavity is resonant at approximately the thousandth mode at 35 kMc/sec. An approximate upper limit to the cavity Q is obtained by a comparison of the total wall area of the cavity to the cross-sectional area of the waveguide; this results in a limiting Q of 500, so that the cavity should be resonant at all frequencies near 35 kMc/sec. Enough modes should be present that the crystals are fairly uniformly illuminated by microwave power.

The cavity and waveguide are suspended from the cover flange of the helium reservoir. A vacuumtight seal isolates the waveguide parts inside the cryostat from the atmosphere.

The associated microwave equipment, all of which is outside the cryostat, consists of:

(a) An isolator, which protects the signal generator from damage due to power reflected back into it.

(b) A variable attenuator, to regulate the amount of power going to the cavity.

(c) A 20-dB branch on which one can monitor the power output and measure the frequency with a calibrated cavity wavemeter.

(d) A 20-dB branch looking at the reflected power, on which one can observe the change in cavity Q at the electron resonance.

(e) A remotely controlled solenoid-operated switch which can direct the microwave power into the cavity or into a dummy load.

The change from positive to negative enhancement of polarization or vice versa can be effected either by changing the microwave frequency (keeping the field fixed) or by changing the field at fixed frequency. The latter method was used during the experiment. Although the klystrons are mechanically

tunable over a small frequency range, frequent tuning is not recommended, nor was it convenient. Each klystron was tuned to a frequency at which it operated stably and with an acceptable power output and was subsequently operated at constant frequency.

C. Detection, Measurement, and Calculation of the Target Polarization

1. General Considerations

The nuclear magnetic resonance of the free-proton spins in the external dc magnetic field is used to detect and measure the free-proton polarization. The state of the proton spin system can be described by a set of magnetic quantum numbers m_i, one for each free proton; any one proton may have $m_i = \pm 1/2$, according to whether its magnetic moment (and spin) is parallel or antiparallel to the external field H_0. The energy levels of the two possible magnetic quantum states are separated by the nuclear Zeeman energy $\delta = g_n \beta_n H_0$, where β_n is the nuclear magneton and g_n is the free-proton spectroscopic splitting factor (see Fig. 1). Transitions between the two Zeeman levels are induced by an applied rf field of frequency δ/h. If the two levels are unequally populated (i.e., if there is a net proton polarization), the proton spin system exchanges energy with the applied rf field. Whether the spin system absorbs energy from the rf field or transfers energy to it depends on which quantum state has the larger population; the applied rf field always tends to equalize the populations. The rate of energy exchange is proportional to the inequality in the populations, a fact which will be further discussed in Sec. II.C.4.

The perturbation due to the rf field is represented by the Hamiltonian

$$\mathcal{H}_{rf}(t) = -g_n\beta_n\vec{I} \cdot \vec{H}_{rf} = -g_n\beta_n(I_xH_{1x} + I_yH_{1y} + I_zH_{1z}) \cos \omega t \qquad \text{(II-4)}$$

where I is the proton spin and $\omega = \delta/\hbar$. If the axis of quantization (i.e., the direction of H_0) is taken as the z axis, the only terms in Eq. (II-4) giving rise to transitions $m = -1/2 \rightarrow m = +1/2$ are those containing $I_\pm = I_x \pm iI_y$. Thus, only the x and y components of H_{rf}, i.e., the components perpendicular to H_0, are effective in inducing the transitions $\Delta m = \pm 1$.

2. Q-Meter Detection

To observe and measure the energy exchange between spin system and rf field, a Q-meter detector[10] is used. The target crystals are placed inside a coil which is supplied with rf current near the resonance frequency by a signal generator. The coil is placed so that the rf magnetic field is perpendicular to H_o, and is resonated at the driving frequency with a variable shunt capacitor. The tuned circuit, which has a characteristic quality factor Q, is isolated from the signal generator by a high impedance, effectively making the latter a constant-current source. When the proton spin system absorbs energy from or transmits energy to the rf field, the effective Q of the tuned circuit is lowered or raised, respectively. This shows up as a change in the voltage across the tuned circuit as the driving frequency is passed through the proton magnetic resonant frequency.

3. Measurement Apparatus

A block diagram of the detection and measurement apparatus is shown in

Fig. 12. The signal generator, a Hewlett-Packard 608C, feeds the tuned circuit through a large capacitive reactance X_s. The reason for choosing a capacitor rather than a resistor of equal impedance is that the thermal noise of the capacitor is far smaller. Since at this point the rf signal from the coil has not yet been amplified, it is critical to keep the noise level as low as possible. For the magnetic field of 9100 G used during the experiment, the NMR frequency is 38.5 Mc/sec.

The rf coil is shown in Fig. 11. It consists of two rectangular "figure eights" in series. Because the skin depth at 38.5 Mc/sec is much less than the 0.002-in. thickness of the microwave cavity, the coil is inside the cavity. The figure-eight construction is used in order to provide a return path for the rf magnetic flux lines. The septum down the middle of the cavity is to steer the magnetic flus lines as indicated in Fig. 11 and provide a more nearly uniform vertical component of the rf field in the region of the crystals. This component was measured and found to vary by a factor of less than 2 over the volume of the crystals.

No hydrogenous materials are used inside the microwave cavity, to avoid picking up a spurious NMR signal. The two crystals on each side of the septum are stuck together with Kel-F fluorinated grease, the rf coil is Teflon-insulated bare copper wire, and the whole package is tied together with Teflon string. It rests on a 1/2-in.-high thin Teflon pedestal at the bottom of the cavity.

The rf coil is joined to the rest of the circuit by a length of coaxial cable which is an integral number of half-wavelengths, and which therefore does not change the tuning of the circuit. The coax leaves the cryostat

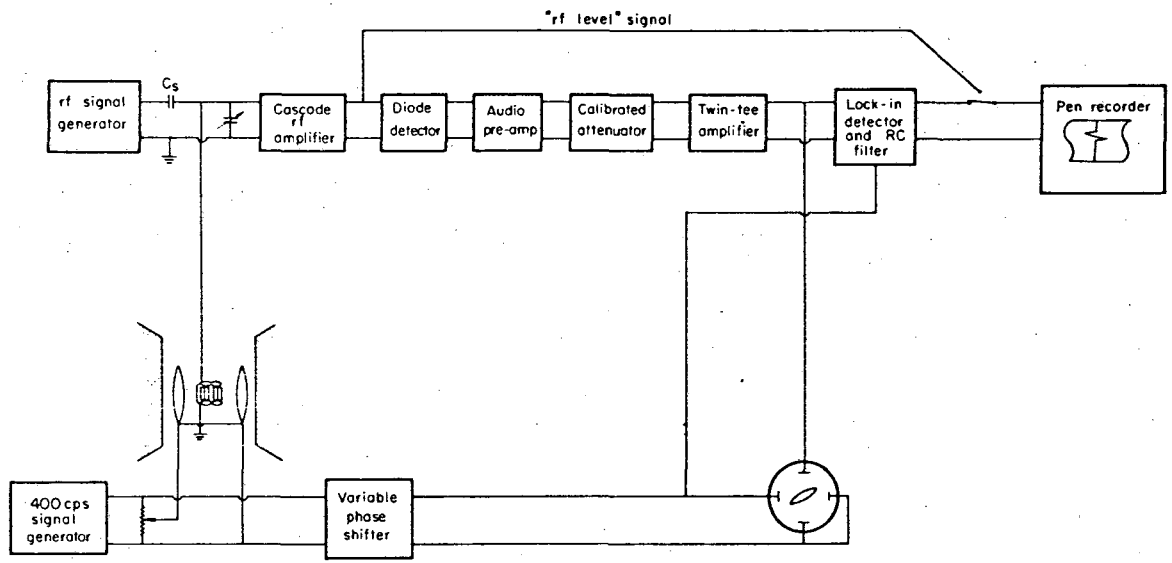

Fig. 12. Schematic diagram of the Q-meter detector.

MUB-2257

through the cover flange, and the rest of the circuit is nearby, to minimize pickup. To minimize heat conduction to the liquid helium, the coax is subminiature (less than 1/8 in. o.d.). To prevent mangetic forces on the coax, the inner conductor is cadmium bronze; this also minimizes the heat leak into the cryostat.

The rf voltage across the resonant circuit is amplified by two cascode low-noise tuned amplifiers in series, with a combined bandwidth of several Mc/sec and a combined gain of 400 at 38.5 Mc/sec. In order to facilitate observation of the change in rf voltage due to the proton spin resonance, H_0 is modulated at 400 cps, so that the resonance manifests itself as a 400-cycle amplitude modulation of the rf voltage. This modulation is effected through a pair of coils of approximate Helmholtz geometry placed in the magnet gap, driven by a 3-W af signal generator. In order to maintain the magnetic field stability required for dynamic polarization, the field modulation is limited to about 1 G peak-to-peak.

The modulated rf voltage is rectified and synchronously detected in a standard way. The diode passes a 400-cps signal proportional to the modulation of the rf carrier voltage. Since the resonance line is $\approx$ 15 G wide, the signal is sinusoidal and proportional to the slope of the resonance line at the carrier frequency.

The 400-cycle signal is then successively passed through an amplifier, a calibrated attenuator, two twin-tee narrow-band amplifiers with 400 cps center frequency, and into a lock-in detector,[11] in which the desired 400-cycle signal adds coherently, while random noise and signals at other frequencies are suppressed by the integrating filter if the time constant is sufficiently long. The reference signal for the lock-in detector is

derived from the same signal generator that drives the field-modulation coils, with an adjustable phase. The signal out of the lock-in detector is a dc signal proportional to the incident ac signal amplitude. The calibrated attenuator is used to keep the signal at a proper level for the recorder, as well as to keep the intermediate amplifiers working in a constant amplitude range.

As the rf carrier frequency is swept across the NMR frequency by a motor drive on the signal generator frequency control, the resulting dc signal is displayed on a millivoltmeter chart recorder, tracing out the derivative of the resonance line. The signal-to-noise ratio varies with the square root of the integrating filter time constant.[11] The time constant must be chosen short enough, however, to ensure that the response follows the variations in signal amplitude. A time constant of 0.5 sec, for a resonance line traversal of 1 min, was found adequate.

In addition to the derivative of the proton resonance line, a signal proportional to the dc current through the diode detector is also recorded. The time constant is long enough so that the 400-cycle modulation does not appear. Assuming an ideal diode (current proportional to rf voltage incident), this signal is proportional to the voltage across the rf coil. As will be explained in the next section, this signal (called the "rf level") is used in the calculation of the polarization of the free protons.

4. Calculation of the Polarization

The polarization of the free protons in the target is measured by observing the size of the NMR signal. Explicit formulae for this are developed in this section. First, some general comments are in order.

The NMR signal depends not only on the polarization, but also on various instrumental parameters such as the coil-filling factor (the fraction of the rf-coil volume filled by the target), the Q of the coil, the average rf magnetic field in the coil, and the amplification in the detection system, some of which cannot be measured accurately or reliably enough to be useful for a direct calculation of the polarization. The detection system is calibrated by measuring the NMR signal at thermal equilibrium with the surrounding liquid helium bath. The polarization at thermal equilibrium can easily be calculated from a knowledge of the external magnetic field and the helium temperature.

The calculation of the polarization then proceeds in two steps. First, a comparison of the NMR signal sizes under conditions of high polarization and at thermal equilibrium gives the enhancement factor E. Secondly, the thermal equilibrium polarization P_0 is calculated. Then the target polarization is $P_T = EP_0$.

Consider the two proton-spin energy levels of Fig. 13, with energies E_+ and E_- and populations N_+ and N_-. The energy difference gives the resonant angular frequency by the relation

$$\delta = E_- - E_+ = \hbar\,\omega_0. \qquad \text{(II-5)}$$

Actually, interactions between neighboring protons cause small variations in the local magnetic field and consequently a distribution of states peaked around E_+ and E_-. The resonance has a finite width and is conventionally described by a line shape function $g(\omega)$, which is a bell-shaped curve peaked

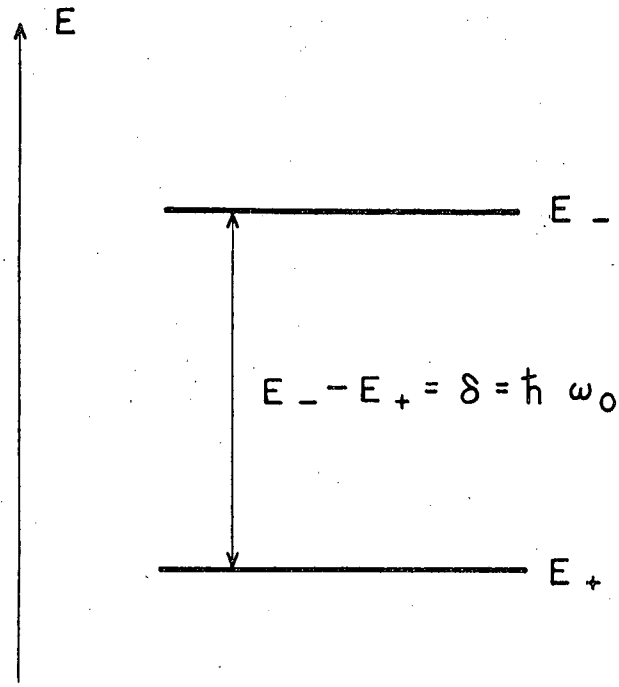

MU-32733

Fig. 13. Energy levels of a free proton in a magnetic field.

around the center frequency ω_0, and which is normalized so that

$$\int_0^\infty g(\omega)d\omega = 1. \qquad \text{(II-6)}$$

Under the action of an applied rf field,

$$H_{rf} = H_{1x} = 2H_1 \cos \omega t = 2\mathrm{Re}(H_1 e^{i\omega t}), \qquad \text{(II-7)}$$

the transition probability between the two states in Fig. 13 is[12]

$$W = \pi/2 \; g(\omega) \; (\gamma H_1)^2 \qquad \text{(II-8)}$$

where γ is the free-proton gyromagnetic ratio. The power absorbed by the spin system is then

$$\text{Power absorbed} = (N_+ - N_-)W\hbar\omega. \qquad \text{(II-9)}$$

Recalling the definition of proton polarization, Eq.(II-1), this becomes

$$\text{Power absorbed} = NP_T W\hbar\omega = \pi/2 \; g(\omega)(\gamma H_1)^2 N\hbar\omega P_T \; , \qquad \text{(II-10)}$$

where N is the total number of protons and P_T is the target polarization.

To obtain expressions more directly related to experimentally observed quantities, a complex rf susceptibility $\chi = \chi' - i\,\chi''$ is introduced, with the usual definition $M_x = \chi H_{1x}$. Here χ' and χ'' represent the

components of the transverse magnetization in phase and 90° out of phase with the transverse rf field, and are called the dispersion and absorption, respectively.

The formula for the power absorbed in terms of the susceptibility now follows in a straightforward manner. From the definition of M_x and Eq.(II-7) one has

$$M_x = 2\mathrm{Re}(\chi H_1 e^{i\omega t}). \tag{II-11}$$

With the usual formula for the power absorption per unit volume,

$$\frac{\text{Power absorbed}}{\text{unit volume}} = \left\langle -\vec{M} \cdot \frac{d\vec{H}}{dt} \right\rangle = -\left\langle M_x \frac{dH_{1x}}{dt} \right\rangle, \tag{II-12}$$

one obtains the result

$$\frac{\text{Power absorbed}}{\text{unit volume}} = 4\omega H_1^2 \chi' \left\langle \sin \omega t \cos \omega t \right\rangle + 4\omega H_1^2 \chi'' \left\langle \sin^2 \omega t \right\rangle$$

$$= 2\omega H_1^2 \chi''. \tag{II-13}$$

Equating (II-10) and (II-13), one has

$$P_T = \frac{4\chi''(\omega)}{\pi\hbar\gamma^2 g(\omega) N_v}, \tag{II-14}$$

where N_v is the number of free-proton spins per unit volume. For the present purpose, it is sufficient to know that the polarization is proportional to χ''.

A relation will now be developed between χ'' and the voltage across the rf coil. It is assumed that a sufficiently large impedance is inserted between the rf signal generator and the tuned circuit to make the current passing through the latter constant to at least that accuracy with which it is desired to know the polarization. In that case the voltage v_{rf} across the coil is proportional to the absolute value of the tuned-circuit impedance. In the absence of any nuclear absorption, the impedance is given by

$$1/Z_o = 1/(R + i\omega L) + i\omega C \ , \qquad \text{(II-15)}$$

where R is the resistance of the coil and coax, L is the inductance of the coil, and C is the shunt capacitance.

To obtain the formula for the impedance of the tuned circuit in the presence of nuclear absorption or emission, use is made of the following argument:[13] the rf field in the coil is made by a current $\mathrm{Re}(Ie^{i\omega t})$. The flux through the coil in the absence of proton spin resonance is

$$\phi = BA = HA = \mathrm{Re}\ (LIe^{i\omega t}), \qquad \text{(II-16)}$$

where A is the area of the coil. In the presence of a transverse magnetization $M_x = \mathrm{Re}(\chi H_{1x})$ in a fraction η of the coil volume, the flux becomes

$$\phi = BA = (H + 4\pi M)A = \mathrm{Re}(LIe^{i\omega t}) + 4\pi\eta\mathrm{Re}(\chi LIe^{i\omega t})$$

$$= \mathrm{Re}\left[L(1 + 4\pi\eta\chi)e^{i\omega t}\right] . \qquad \text{(II-17)}$$

Effectively, in the presence of nuclear magnetization, the inductance of the coil takes the complex value $L(1 + 4\pi\eta\chi)$. Thus, the generalized version of Eq. (II-15) becomes

$$\frac{1}{Z} = \frac{1}{R + i\omega L(1 + 4\pi\eta\chi)} + i\omega C . \qquad \text{(II-18)}$$

At this point it is necessary to jump slightly ahead in this exposition and consider for a moment the accuracy to which it is desired to know the polarization. The dominant source of error in this experiment was the statistical error on the scattering asymmetry, which ranged from 25% to more than 100%. Since the fractional error of the target polarization is added in quadrature, this polarization need be known only to about 10%. This will be of considerable help in simplifying the calculation of the polarization.

In solving Eq. (II-18) for Z, use is made of the relationship between ω, L, C, and R in a parallel resonant circuit to simplify the resulting formula. It will be remembered that the conventional definition of the resonant frequency is that frequency for which Z_0 is purely resistive, and that this frequency is[14]

$$\omega_{res}^2 = \frac{1}{LC} - \frac{R^2}{L^2} \approx \frac{1}{LC}\left(1 - \frac{1}{Q^2}\right), \qquad \text{(II-19)}$$

where $Q = \omega L/R$ is the quality factor of the circuit. In actual practice, however, the variable capacity C is adjusted not so that Z_0 is real, but so that the voltage across the coil, v_{rf}, is maximum -- i.e., so that $|Z_0|$ is maximum. If one solves for ω_{max} so that $|Z_0|$ is maximum, one

obtains

$$\omega_{max}^2 = -\frac{R^2}{L^2} + \frac{1}{LC}\sqrt{1+\frac{2}{Q^2}} \approx -\frac{R^2}{L^2} + \frac{1}{LC}\left(1+\frac{1}{Q^2}\right) \approx \frac{1}{LC} \qquad \text{(II-20)}$$

to a fractional accuracy of $1/Q^4$. Since coil Q's are typically between 10 and 100, Eq. (II-20) is adequate not only for the modest requirements of this experiment but for much more accurate measurements as well.

Equation (II-20) can be used to simplify the expression for Z resulting from Eq. (II-18):

$$Z = \frac{\omega^2 L^2}{R}\left[\frac{1+4\pi\eta\chi - i/Q}{1+4\pi i\eta Q\chi}\right] \qquad \text{(II-21)}$$

where ω^2L^2/R is the (real) impedance of a parallel-resonant circuit. Since $Q \gg 1$, and $4\pi\eta\chi \ll 1$ even for large polarizations,

$$Z \approx \frac{\omega^2L^2}{R}\,\frac{1}{1+4\pi i\eta Q}\,. \qquad \text{(II-22)}$$

If, in addition, $4\pi\eta\chi' Q \ll 1$,

$$|Z| \approx \frac{\omega^2L^2}{R}\,\frac{1}{1+4\pi\eta Q\chi''}\,, \qquad \text{(II-23)}$$

since a small imaginary part has little effect on $|Z|$.

For convenience the substitution

$$\varphi = \varphi' - i\varphi'' \equiv 4\pi\eta\omega L(\chi' - i\chi'') \tag{II-24}$$

is used hereafter. Then Eq. (II-23) becomes

$$Z = (\omega L)^2/R + \varphi'' \ . \tag{II-25}$$

The signal actually recorded is proportional to

$$\frac{\partial |Z|}{\partial H_0} = -\frac{(\omega L)^2}{(R+\varphi'')^2}\frac{\partial \varphi''}{\partial H_0} = -\frac{|Z|^2}{(\omega L)^2}\frac{\partial \varphi''}{\partial H_0} \tag{II-26}$$

Equation (II-26) is the basis for the usual statement that a Q-meter detector is linear in the polarization. If the shape of $\chi''(\omega,H_0)$ is independent of the polarization, then $\partial\varphi''/\partial H_0$ is as good a measure of the polarization as φ''. If, in addition, the relative change in Z due to the resonance is small (i.e., if $\Delta Q/Q \ll 1$), then $\partial|Z|/\partial H_0$ is proportional to the polarization. Both conditions are satisfied at sufficiently low target polarizations, but at $P_T \approx 20\%$ deviations from linearity occur. The deviation due to the nonzero change in Q can be avoided by noting that $\partial\varphi''/\partial H_0$ is proportional to $\frac{1}{|Z|^2}\,\partial|Z|/\partial H_0$.

In the analysis of this experiment the magnitude of $\frac{1}{|Z|^2}\,\partial|Z|/\partial H_0$ was used as a measure of the polarization, and a correction was added for the change in line shape. The magnitude of $\partial|Z|/\partial H_0$ was measured as the peak-to-peak amplitude of the signal traced out as a function of rf frequency. (The signal, being roughly proportional to the derivative of the bell-shaped

function ϕ'' , has the general appearance of a dispersion curve, with peaks at the points of maximum slope of ϕ''.) A signal proportional to $|Z|$ is obtained from the "rf level" signal mentioned in Sec. II.C.2. The proper procedure is to divide each peak amplitude of $\partial|Z|/\partial H_0$ by $|Z|^2$ measured at the same frequency. Since the value of $|Z|$ at the position of maximum slope is difficult to read from a graph of $|Z|$ vs. ω , and since it is about halfway between $|Z_0(\omega_0)|$ (the "base line") and $|Z(\omega_0)|$ (the value at the center of the resonance), the procedure generally adopted was to divide the peak-to-peak amplitude of $\partial|Z|/\partial H_0$ by the product of $|Z_0(\omega_0)|$ and $|Z(\omega_0)|$. Since, at $P_T \simeq 20\%$, $|Z_0(\omega_0)|$ and $|Z(\omega_0)|$ differ by only 6%, this procedure is adequate for the desired accuracy. At thermal equilibrium polarization (0.07% during the experiment), the signal-to-noise ratio is such that no difference can be detected between $|Z_0|$ and $|Z|$.

The rf level signal also provides a foolproof way to determine the direction of $\vec{P}_T$: if $|Z|$ decreases at resonance, one has nuclear absorption, the protons are predominantly in the lower-energy state, and $\vec{P}_T$ is parallel to $\vec{H}_0$: this is called positive enhancement. Conversely, if $|Z|$ increases at resonance, $\vec{P}_T$ is antiparallel to $\vec{H}_0$, and the enhancement is negative.

To take proper account of the change in resonance line shape with polarization, a formalism is developed that does not depend on a detailed knowledge of the line shape function $g(\omega)$, but uses instead its normalization, Eq. (II-6):

$$\int_0^\infty g(\omega)\, d\omega = 1$$

Since, by Eq. (II-14), $\chi''(\omega)$ [and consequently also $\varphi''(\omega)$] is proportional to $g(\omega)$, and to P_T,

$$\int_0^\infty \varphi''(\omega)d\omega = P_T \times \text{ constant independent of polarization.} \qquad \text{(II-27)}$$

[Although, strictly speaking, $\varphi''(\omega) \propto \omega\, \chi''(\omega)$, the region in which $g(\omega)$ is nonzero is so small compared with ω (100 kc/sec vs. 40 Mc/sec)that the factor ω can be safely taken outside the integral.] The functional dependence of the absorption $\varphi''(\omega, H_0)$ is always of the form $\varphi''(\omega - \gamma H_0)$. Hence,

$$\frac{\partial\varphi''}{\partial H_0} = -\gamma \frac{\partial\varphi''}{\partial\omega} . \qquad \text{(II-28)}$$

Using Eqs. (II-26) and (II-38), one can form the double integral

$$\int_0^\infty d\omega'' \int_0^{\omega''} d\omega' \frac{1}{|Z(\omega')|^2} \frac{\partial|Z(\omega')|}{\partial H_0} = \frac{\gamma}{(\omega L)^2} \int_0^\infty d\omega'' \varphi''(\omega'') , \qquad \text{(II-29)}$$

which, by Eq. (II-27), is proportional to P_T.

The calculation of target polarizations by use of this prescription can obviously be a very time-consuming operation if done manually. Furthermore, a linear (or at least a calibrated) frequency-driving mechanism is needed, and the chart recorder paper speed must be such that the signals are accurately readable at small frequency intervals. In the analysis of this experiment, this operation was performed on one occasion, and the result compared with that of the simpler calculation, using the same thermal

equilibrium and enhanced signals. In this way, a correction factor of 0.85 was obtained, which was applied to all other calculated polarizations.

The recorded signals are proportional to $\frac{\partial|Z|}{\partial H_0}$ and $|Z|$ only to the extent that the series current through the tuned circuit is constant. This current is given by

$$I_s = \frac{V_{osc}}{|\vec{X}_s + \vec{Z}|} , \qquad \text{(II-30)}$$

where V_{osc} is the rf signal generator voltage, and $\vec{X}_s$ is the reactance of the series capacitor. The requirement for constant I_s is that $|X_s|$ be much larger than the change in $|Z|$ due to the nuclear magnetism. Measurements indicate that during the experiment the change in I_s due to nuclear magnetism was less than 1%.

5. Measurement Procedure

Several auxiliary measurements were made to ensure linearity of the detection system. The various amplifiers were checked for their regions of linearity, and the signals were kept in these regions. The signal attenuator was calibrated and found to agree with the nominal attenuation values to better than 1%. The frequency of the audio oscillator was monitored to ensure that it stayed on the peak of the twin-tee response curve. The phase of the lock-in detector reference signal was monitored to ensure that it remained in phase with the $\partial|Z|/\partial H_0$ signal. The frequency response of the rf amplifier stages was found to be flat within the desired accuracy of this experiment.

The only nonlinearity in the detection system is in the diode detector, which was found to have a nonlinear current-vs-voltage curve in the region in which it was used. The diode response curve was measured by recording the "rf level" appearing at the chart recorder -- and proportional to the diode current -- as a function of input rf voltage as measured by an rf voltmeter. This gives a calibration of the "apparent rf level," hereafter called W, vs the "true rf level," V_{rf}. Since $|Z| \propto V_{rf}$, all rf levels read on the recorder were changed to true rf levels by means of the calibration curve before being used in calculations. Similarly, the differential signal as read at the recorder is $\partial W/\partial H_0$ rather than $\partial V_{rf} / \partial H_0$, and was corrected by the factor $\partial V_{rf} / \partial W$, i.e., by the slope of the calibration curve, before being used in calculations. (Since the polarization is calculated by comparing the enhanced and thermal equilibrium signals, V_{rf} and $\partial V_{rf} / \partial H_0$ in any consistent set of units can be used in place of $|Z|$ and $\partial |Z| / \partial H_0$.)

Clearly this requires the simultaneous recording of $\partial W(\omega)/\partial H_0$ and $W(\omega)$. In practice, since only one recorder was available, they were recorded in succession, at times when the polarization was fairly constant. Since V_{rf} changes by only 6% in going from no polarization to 20% polarization, this procedure was adequate.

A measurement of the target polarization is meaningful only if the act of measuring does not significantly affect the polarization. At thermal equilibrium, the spin system, under the combined action of thermal relaxation tending to polarize it to a value $P_0 = \tanh \delta/2kT$ and of rf-induced transitions tending to depolarize it, arrives at a steady-state polarization[15]

$$P_T = P_0/1 + (\gamma H_1)^2 T_1 T_2 , \qquad \text{(II-31)}$$

where T_1 is the longitudinal relaxation time, the characteristic time in which the spin system exponentially approaches thermal equilibrium polarization in the absence of an rf field; $P_T = P_0$ if $(\gamma H_1)^2 T_1 T_2 \ll 1$; T_1 was measured and found to be of the order of 10 minutes; and $1/T_2 = 2\pi$ (half-width at half-maximum of the resonance line) $\approx 2 \times 10^5$ sec^{-1}. Thus, the requirement is

$$\gamma H_1 \ll 20 \text{ sec}^{-1} . \qquad \text{(II-32)}$$

Remembering the field-frequency conversion $4.26 \ \frac{\text{kc/sec}}{\text{G}}$, this yields

$$H_1 \ll 5 \times 10^{-3} \text{ G} .$$

Estimates of H_1 made from an approximate knowledge of the series current I_s and of the coil Q lead to a value of H_1 less than 1×10^{-3} G. That the presence of H_1 does not affect the polarization significantly is experimentally verified by comparing signal sizes immediately after the rf frequency has been at ω_0 for several minutes and after it has been off resonance for several minutes. No change in amplitude was found, either at thermal equilibrium or at enhanced polarizations.

On a given day the measurement procedure is as follows: about one hour before data taking is to begin, the cryostat is filled with liquid

helium, and the target allowed to come to thermal equilibrium. The differential signal is monitored during this time, and when it stops growing, the polarization is at its thermal equilibrium value. This generally takes about 15 min. The differential signal and rf level are then recorded several times; a typical differential signal is shown in Fig. 14.

Frequently the zeroline of the differential signal is displaced from zero voltage on the recorder. This is because of the buckling of the thin walls of the microwave cavity when the 400-cycle eddy currents due to the field modulation interact with H_0 . This slightly changes the inductance of the rf coil and causes an additional 400-cycle modulation of the rf voltage across the coil, and a 400-cycle signal at the lock-in detector. The amplitude and phase of this signal change from day to day, but remain the same on a given day once the temperature is fairly constant. The resulting dc signal at the recorder often changes with rf frequency, causing a curved but reproducible effective zero line. When the zero line is quite sloped, and its position somewhat uncertain, the "potato," as it is called because of its shape when displayed on a synchronously swept scope screen, can be separately recorded by changing H_0 a small amount, just enough to move the proton resonance away from the frequency region of interest. If the potato is so large as to make the NMR signal difficult to measure, one can trace the latter out by sweeping H_0 instead of the frequency (thereby at least making the potato constant), and offsetting the zero at the recorder to bring the signal on scale. However, if possible, it is preferable to measure the unenhanced and enhanced signals in exactly the same way. (The signal at high polarization cannot be measured by field-sweeping because

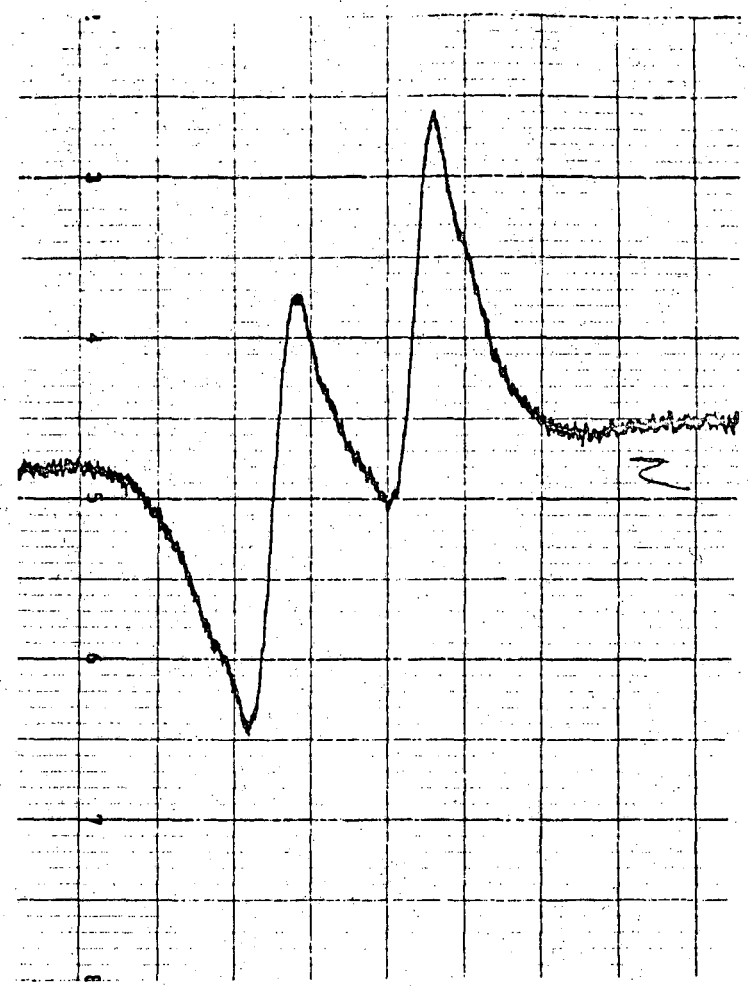

MU-32736

Fig. 14. Typical differential signal at thermal equilibrium polarization.

that would change the polarization.)

For the purpose of calculating the thermal equilibrium polarization, the field H_0 is measured by measuring the center frequency of the proton resonance, and the temperature is measured by measuring the vapor pressure of the liquid helium bath with an oil manometer. At $H_0 = 9100$ G and $T = 1.2^{\circ}K$, the thermal equilibrium polarization is about 0.07%.

The measurement of enhanced signals is carried out in much the same way. The rf frequency is swept back and forth through the proton resonance line, providing a semicontinuous monitor of the amplitude of $\partial W/\partial H_0$. Occasionally $W(\omega)$ is recorded instead, for use in calculating some of the corrections to the polarization. The polarization is calculated by using adjacent $\partial W(\omega)/\partial H_0$ and $W(\omega)$ signals, and each of these calculations is used as a calibration point; the polarization corresponding to any other differential signal is assumed to be proportional to its peak-to-peak amplitude. Since enhanced signal sizes did not vary by more than 10 or 20% over the time spans involved, this assumption is justified. The average target polarization for each group of scattering data known as a "run" (see Section IV.F.4) was calculated from the average peak-to-peak amplitude during the time of that "run."

The signal corresponding to thermal equilibrium polarization is remeasured every few hours (the exact time intervals depend mostly on boundary conditions due to the accelerator schedule and the needs of the scattering experiment), and again at the end of the day--a "day being a period of more or less uninterrupted data-taking, which is usually between 12 and 48 hours long. The various thermal equilibrium signal amplitudes from a day's running are generally found to agree with one another to about 5%. With a normal

signal-to-noise ratio of about 20, the amplitude of each signal can be measured only to about 5%, so that the agreement is not unreasonable.

To obtain the thermal equilibrium signal more quickly than by allowing a signal 300 times as large to decay exponentially with a time constant of 10 minutes, a large rf current at the frequency ω_0 is applied to the coil by circumventing the series capacitor C_s of Fig. 12, causing a large H_1 field at the target. According to Eq. (II-31) a sufficiently large H_1 causes a zero steady-state polarization; in other words, the populations of the two proton spin states are equalized by the high transition probability caused by the large H_1. In practice, the polarization is destroyed by this method in about 3 min. It then grows back to within 10% of its thermal equilibrium value in about twice the relaxation time.

6. Polarization Results

During the scattering experiment, the average target polarization was 22%. This was lower than it need have been, for a klystron which was on its last legs was used during most of the experiment. It finally died two days before the end of the experiment, and was replaced by a borrowed klystron of the same kind. Thereafter, the polarization averaged 25%, and on some runs was as high as 27%. Slightly higher polarizations could probably have been obtained by increasing the microwave power supplied to the target, but at the expense of a higher rate of liquid helium consumption and therefore more frequent interruptions in the data-taking.

During normal operation, liquid helium refills must be made every 4 hours. It takes about 20 minutes to refill and bring the polarization back up to a high level.

During a true steady state, the target polarization is quite constant, but changes in the microwave power, drifts of the magnetic field, the need to refill helium, and the frequent reversals of the polarization direction required by the scattering experiment make prolonged steady-state operation a rare luxury.

Under ideal conditions it is possible to measure the polarization with a fractional uncertainty of less than ± 5%. The principal source of error is uncertainty of the thermal equilibrium signal due to the small signal-to-noise ratio.

D. Recent Improvements in the Polarized Target

The reader may have noticed the frequent vacillation between present and past tense in the preceding sections dealing with the polarized target. The reason is that since the end of the scattering experiment that is the main subject of this dissertation (March 1963), a number of important changes have been made in the construction and operation of the polarized target and its associated equipment, resulting in great improvement in the polarization and in other areas.

By far the most important change is the switch to microwave tubes oscillating at 70 kMc/sec, twice the former frequency, and a commensurate change in magnetic field to 18 800 gauss. These changes have brought the target polarization to values consistently over 60%, and occasionally as high as 65% (vs a theoretical limit of 88%). Only a part of the increase in polarization is due directly to the increase in microwave frequency; the rest is due to the improved resolution of the partially forbidden electron spin resonance. In the best cases, three-quarters of the theoretically possible polarization is achieved, as opposed to half at 9100 G.

The 70-kMc/sec radiation is obtained from a Carcinotron COE-40 backward-wave oscillator, capable of putting out 10 W CW . Although most of the microwave system has been switched to 4-mm components, the waveguide inside the cryostat and the cavity are unchanged. The 8-mm waveguide was retained because it is far less lossy than 4-mm waveguide; the fact that it probably does not transmit a pure mode is of no concern, since the cavity is untuned.

The operation of the target is considerably simplified by the circumstance that Carcinotrons are electronically tunable over a range of 3 kMc/sec. The magnetic field and the NMR frequency are held fixed and the microwave frequency is varied to obtain the optimum polarization, or to reverse the direction of polarization. This has led to the technique of "sitting on the peak" (keeping the NMR frequency fixed so that the differential signal is at one of its peaks), where small changes in polarization can be rapidly detected, thereby considerably speeding up the optimizing of the polarization.

The proton relaxation time T_1 is now 15 to 20 min (vs 10 min at 9100 G), which makes the approach toward thermal equilibrium much slower, and the measurement of the thermal equilibrium signal much more time-consuming.

With the achievement of such high polarization, the question of the validity of the approximations used in deriving the formulae for calculating the target polarization must be reopened. In particular, the fractional change in Q , as measured by the fractional change in $|Z|$, is now 25%; and the line shape changes drastically between thermal equilibrium and 60% polarizations, as can be seen by comparing the differential signals in Figs. 14 and 15. Expressions for calculating the polarization under these conditions are developed in the Appendix.

The true resonance line shapes

$$\int_0^{\omega} d\omega' \frac{1}{|Z(\omega')|^2} \frac{\partial |Z(\omega')}{\partial \omega'} ,$$

as obtained from actual data, are shown in Fig. 16 for thermal equilibrium, for large positive, and for large negative polarization, and provide an interesting qualitative explanation of the line shape. Consider two protons, the hydrogen nuclei of a water molecule, spatially arranged as in Fig. 17 with respect to the dc field $\vec{H}_0$. The field at proton 1 is $(\vec{H}_0 + \vec{H}_{21})$, where $\vec{H}_{21}$ is the dipolar field of proton 2 at proton 1:

$$H_{21} = \frac{2\,\vec{\mu}_2}{|\vec{r}_{21}|^3} . \qquad \text{(II-34)}$$

Since $\mu_p \approx 10^{-3}$ Bohr magnetons and $|\vec{r}|_{21} \approx$ a few Angstroms, H_{21} is a few gauss. There are two possible values of the local field at proton 1, differing by a few G, and two resonant frequencies, depending on the spin orientation of proton 2. This structure is seen in Fig. 16(a), where the two peaks are separated by 9 G. In Fig. 16(b), corresponding to high positive polarization, proton 2 is more likely to be parallel to H_0, causing a local field $H_0 + H_{21}$ at proton 1; therefore, the high-frequency peak stands out, while the low-frequency peak shrinks. In Fig. 16(c), for negative polarization, just the reverse is true.

In order to make a cleaner separation between scattering events from the polarized free protons of the target and background events due to scattering

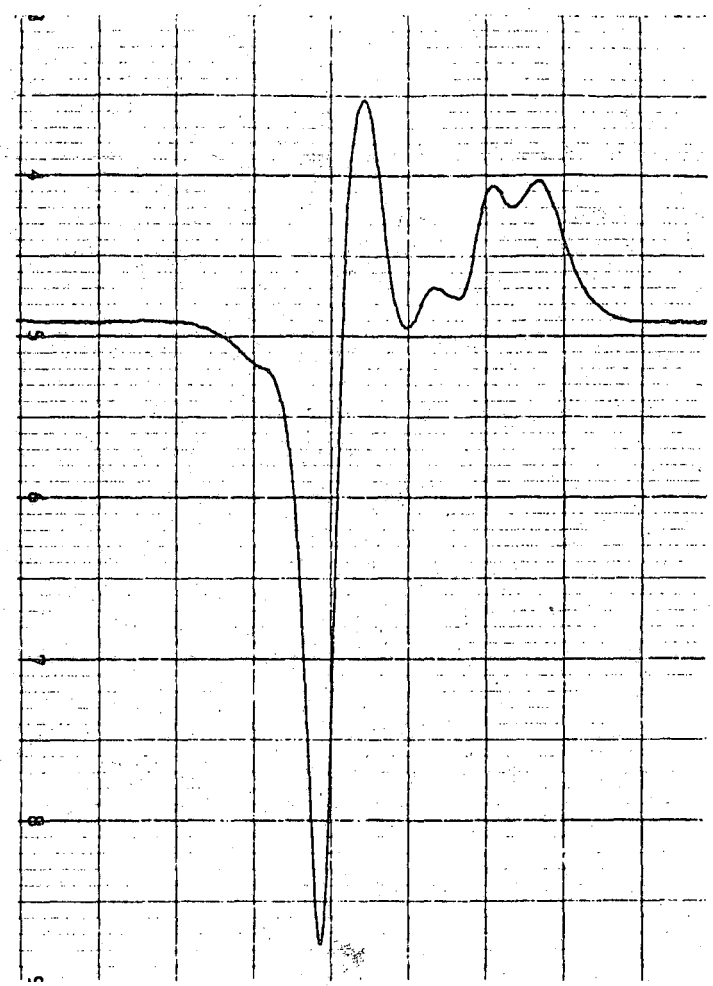

MU-32735

Fig. 15. Typical differential signal at about 60% polarization.

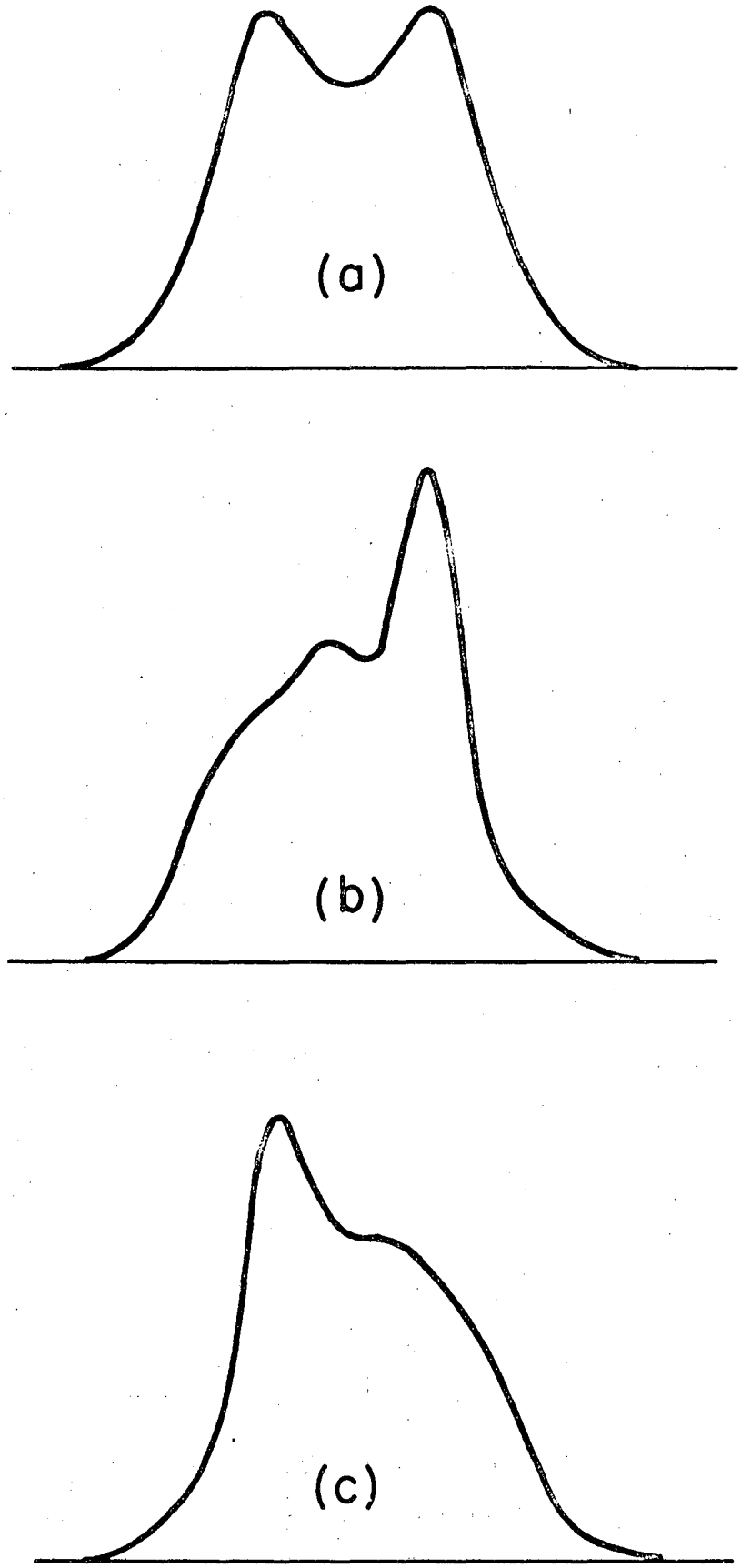

Fig. 16 NMR absorption line shapes, obtained by numerical integration of the properly corrected differential signals: (a) at thermal equilibrium; (b) at high positive enhancement; (c) at high negative enhancement. The three signals are normalized to equal areas.

MU-32816

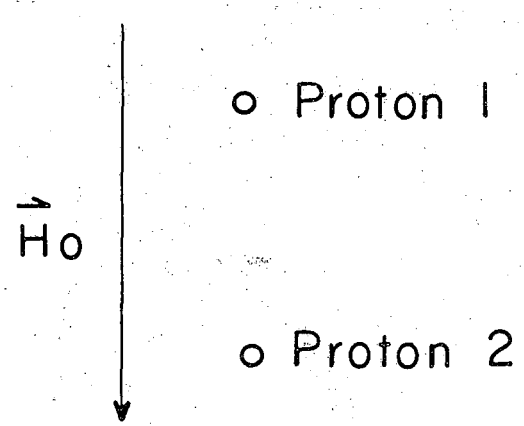

MU-32732

Fig. 17. Model of the spatial arrangement of two free protons in a magnetic field, used to qualitatively explain the double resonance line in Fig. 16.

from the complex nuclei of the target and from the cryostat, the 0.005-in. Mylar flask at the bottom of the helium container and the 0.005-in. Mylar wrap-around window at the bottom of the vacuum can have been replaced by identical parts constructed of 0.003-in. aluminum alloy. This has eliminated a major source of background, scattering events from hydrogen nuclei in the Mylar. The background subtraction is discussed in detail in Sections IV.F.5 and V.A.

III. ELASTIC PION-NUCLEON SCATTERING

It is convenient to describe elastic pion-nucleon scattering through the density matrix formalism.[16] The polarization of a beam of protons is described by a 2-by-2 matrix ρ, the density matrix, given by

$$\rho = 1/2(1 + \vec{\sigma} \cdot \vec{P}), \tag{III-1}$$

where $\vec{\sigma}$ is a vector whose components are the three 2-by-2 Pauli spin matrices, and $\vec{P}$ is a vector whose components are the expectation values of the proton spin (in units of $\hbar/2$) along the three axes of a Cartesian coordinate system. Here ρ is normalized to have unit trace. The expectation value of any operator in the proton spin space is given by

$$\langle \mathcal{O} \rangle = \mathrm{Tr}(\rho \mathcal{O}), \tag{III-2}$$

as, for example, the expectation value of the ith component of the proton spin operator:

$$\langle \sigma_i \rangle = \mathrm{Tr}\ \rho\sigma_i = 1/2\ \mathrm{Tr}(\sigma_i + \vec{P} \cdot \vec{\sigma}\ \sigma_i) = 1/2\ \mathrm{Tr}(P_i\ \sigma_i^2) = P_i\ . \tag{III-3}$$

(Considerable use is made in the remainder of this section of the algebra of the Pauli spin matrices.[17] In particular, use is made of the relations $\sigma_i\sigma_j = i\epsilon_{ijk}\ \sigma_k + \delta_{ij}$ and $\mathrm{Tr}\ \sigma_i = 0$.) The expectation value of the unit matrix is 1, which is equivalent to saying that the beam described by ρ has unit intensity or unit flux.

The scattering of a beam of protons by a spin-zero target is described by a 2-by-2 scattering matrix M, which transforms the incident into the scattered wave function,

$$\psi_{scatt} = M\psi_{inc}, \tag{III-4}$$

where M is a 2-by-2 matrix in the spin space of the protons, and is the analog of the scattering amplitude in the scattering of spinless particles by a central potential.

The density matrix ρ_f of a beam of protons scattered from a spin-zero target is given in terms of the initial density matrix ρ_i by

$$\rho_f = M\rho_i M^\dagger, \tag{III-5}$$

where $M^\dagger$ is the Hermitian conjugate of M. Although the trace of ρ_f is not necessarily unity, this definition is preferable because the formula for the intensity of the scattered beam per unit incident beam (i.e., the differential cross section) is

$$I = \mathrm{Tr}\ \rho_f\ ; \tag{III-6}$$

for an unpolarized incident proton beam, one has

$$I = 1/2\ \mathrm{Tr}(MM^\dagger), \tag{III-7}$$

the form of which is similar to the familiar $I = |f(\theta)|^2$ of the spinless theory. The ith component of the expectation value of the spin of the scattered protons is

$$\langle \sigma_i \rangle = \frac{\mathrm{Tr}(\rho_f \sigma_i)}{\mathrm{Tr}\, \rho_f} = \frac{\mathrm{Tr}(M \rho_i M^\dagger \sigma_i)}{\mathrm{Tr}(M \rho_i M^\dagger)} \quad . \tag{III-8}$$

The most general form of M for the case of a spin-1/2 particle incident on a spin-zero target (which is equivalent to the case of a pion and a proton scattering in the center-of-mass frame) is, assuming parity is conserved in the scattering,[18]

$$M = f(\theta) + g(\theta)\, \vec{\sigma} \cdot \hat{n} \ , \tag{III-9}$$

where

$$\hat{n} = \frac{\vec{k}_i \times \vec{k}_f}{|\vec{k}_i \times \vec{k}_j|} \tag{III-10}$$

is a unit vector perpendicular to the scattering plane ($\vec{k}_i$ and $\vec{k}_f$ are the initial and final momenta of either particle in the center-of-mass system). The quantities $f(\theta)$ and $g(\theta)$ are the non-spin-flip and spin-flip smplitudes, so named because they have exactly those properties if the two pure helicity states are taken as the basis of the proton spin space.

The differential cross section $I_0(\theta)$ of pions from unpolarized protons is given by Eq. (II-7):

$$I_0(\theta) = 1/2 \text{ Tr } \left[(g + h\vec{\sigma} \cdot \hat{n})(g^* + h^* \vec{\sigma} \cdot \hat{n})\right] = |g(\theta)|^2 + |h(\theta)|^2. \quad \text{(III-11)}$$

The $\hat{n}$ component of polarization of the recoil protons from an initially unpolarized target is, by Eq. (II-8),

$$P_n(\theta) = \left\langle \vec{\sigma} \cdot \hat{n} \right\rangle = \frac{\text{Tr } [(g + h\vec{\sigma} \cdot \hat{n})1/2(g^* + h^*\vec{\sigma} \cdot \hat{n})]}{|g|^2 + |h|^2}$$

$$= \frac{2 \text{ Re}[g^*(\theta) \ h(\theta)]}{|g(\theta)|^2 + |h(\theta)|^2} \ . \quad \text{(III-12)}$$

The other two components of the recoil-proton polarization turn out, by the same formalism, to be zero, yielding the familiar result that in a scattering that conserves parity, the polarization, if any, must be perpendicular to the plane of scattering.

Consider now scattering from polarized protons, whose polarization is in the $\hat{n}$ direction,

$$\vec{P}_T = P_T \ \hat{n} \ . \quad \text{(III-13)}$$

The initial density matrix is, by (III-1),

$$\rho_i = 1/2(1 + P_T \vec{\sigma} \cdot \hat{n}) \ . \quad \text{(III-14)}$$

The differential cross section from pions is, by Eq. (III-6),

$$I(\theta) = \mathrm{Tr}\left[(g + h\vec{\sigma}\cdot\hat{n})1/2(1 + P_T\,\vec{\sigma}\cdot\hat{n})(g^* + h^*\vec{\sigma}\cdot\hat{n})\right]$$

$$= |g(\theta)|^2 + |h(\theta)|^2 + 2\,\mathrm{Re}[g^*(\theta)\,h(\theta)] \;\times\; P_T$$

$$= I_0(\theta)[1 + P\vec{P}_T\cdot\hat{n}], \qquad \text{(III-15)}$$

where the "polarization" in π-p scattering is defined by Eq. (II-12),

$$P = \frac{2\,\mathrm{Re}\;g^*h}{|g|^2 + |h|^2} \;. \qquad \text{(III-16)}$$

If counting rates are compared for the two cases $\vec{P}_T = +|P_T|\hat{n}$ and $\vec{P}_T = -|P_T|\hat{n}$, an experimental asymmetry

$$\epsilon = \frac{I_+ - I_-}{I_+ + I_-} = P \times P_T \qquad \text{(III-17)}$$

can be defined. Thus a measurement of the asymmetry in the scattering of pions from polarized protons yields the same parameter P as an analysis of the polarization of recoil protons from an unpolarized target. That this should be so can be explained by the qualitative argument that both measurements are essentially comparisons of the differential cross section for the two cases

$$\langle\vec{\sigma}_P\rangle = +\frac{1}{2}\hbar\,\hat{n} \quad \text{and} \quad \langle\vec{\sigma}_P\rangle = -\frac{1}{2}\hbar\,\hat{n}\;.$$

According to the generally accepted postulate of charge independence, the scattering amplitudes in all possible charge states of the pion-nucleon system can be written in terms of appropriate linear combinations of two independent amplitudes of the form (III-9), one amplitude for total isotopic spin 3/2 and one for total isotopic spin 1/2. The elastic π^+-p reaction, being in a pure isotopic spin-3/2 state, gives information only about the isotopic spin-3/2 scattering amplitude.

IV. THE SCATTERING EXPERIMENT

A. General Considerations

To measure the asymmetry in scattering of pions from polarized protons, one has the choice of two experimental methods. First, one can compare the differential cross section of the process in two directions whose polar scattering angles are equal, and whose azimuthal angles are 0° and 180°. Secondly, one can choose one direction only (fixed polar and azimuthal angles) and compare the differential cross sections for two orientations of the target polarization, preferably such that $\vec{P}_T \cdot \hat{n} = \pm 1$ (cf. Eq. (III-14). It was this second method that was used in the experiment. In this way one avoids the most common systematic error in the usual asymmetry measurement, the misalignment of counters when moving them from one side of the beam to the other.

Since only a small fraction of the charged particles scattered in any direction resulted from elastic pion collisions with the polarized free protons, means had to be found to distinguish these from the larger background of other types of events. In the angular region in which the recoil protons had enough energy to leave the target (backwards of 105° c.m.), a coincidence was required between the detection of the pion and that of its recoil proton at the proper polar angles to satisfy the kinematics of π-p scattering, and the directions of the incident beam and of the two scattered particles were required to be coplanar. Since the nucleons in complex nuclei have momenta of the order of 200 MeV/c, detection of pions scattered from bound nucleons--as well as pions from inelastic, quasi-elastic, and coherent scattering on nuclei--was severely discriminated against by this method.

At smaller c.m. angles, where the recoil protons could not be detected, the correlation of energy with angle of the scattered mesons was used to distinguish the elastic scattering on hydrogen. This was done by placing appropriate upper and lower limits on the range of the scattered pions. This method is inferior to the two-particle coincidence technique, especially since there is no coplanarity requirement. Consequently, the fraction of unwanted events accepted as hydrogen events was larger.

Quantitative methods of determining the amount of background due to complex-nuclear scatterings is discussed in Section IV.F.4.

The scattering geometry is illustrated in Fig. 18. The scattering plane is the vertical, because it proved most convenient to build the polarized target with the magnet gap vertical, and with the target polarization horizontal, making $|\vec{P}_T \cdot \hat{n}| = 1$.

The pion beam entered the magnet gap about 2 in. above center line and was deflected downward so that it passed through the target at the center of the magnet. The scattered pions were detected below the beam line, and the recoil protons above, as shown in Fig. 18.

The pion beam energy of this experiment was chosen to match the energy of a previous experiment,[19] which measured the differential cross section for scattering of positive pions on unpolarized protons.

B. Pion Beam

The external proton beam of the Berkeley 184-inch synchrocyclotron was used to produce the positive π-meson beam used in this experiment. A polyethylene production target, 30.5 in. thick, was placed in the beam of

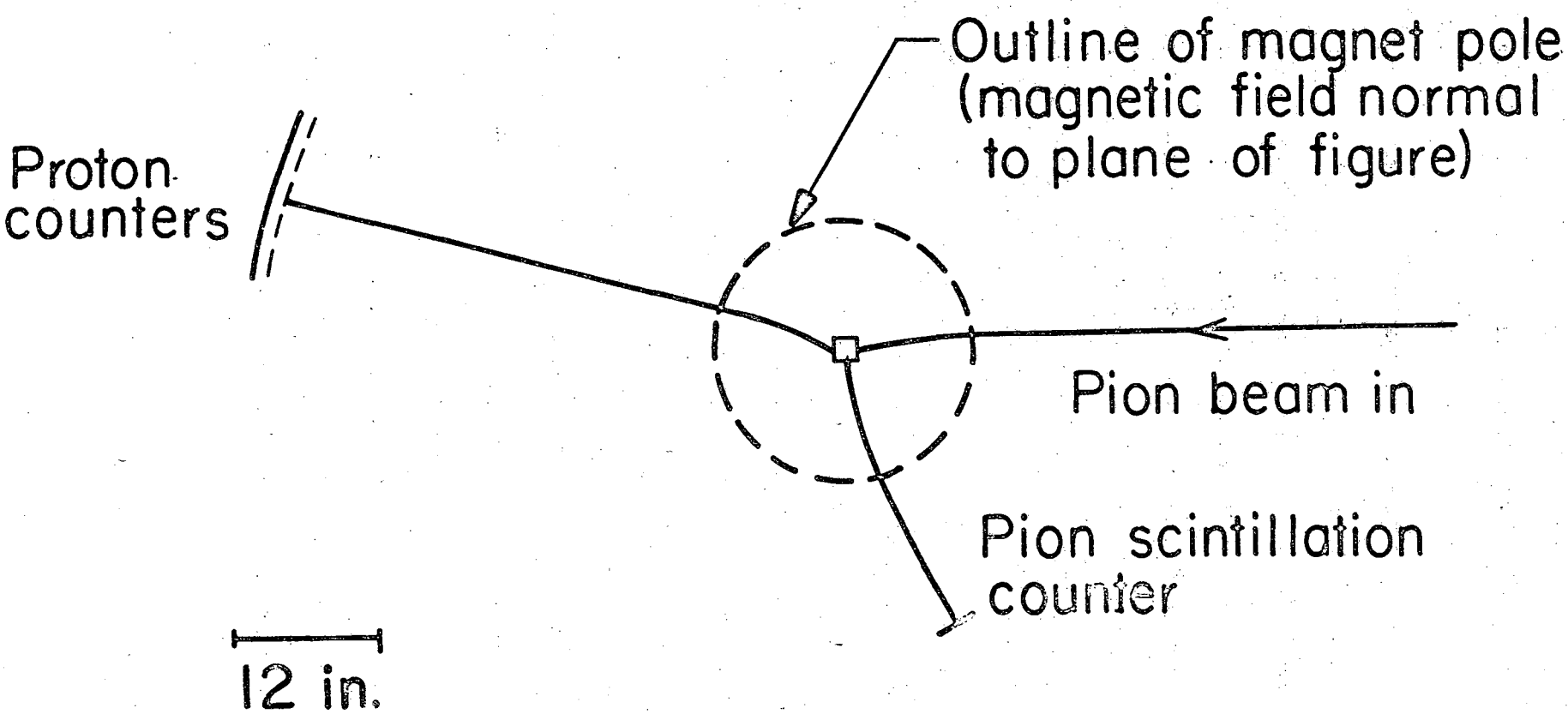

MU-30598A

Fig. 18. Scale diagram of the scattering geometry (elevation view).

protons of 740 MeV kinetic energy, and the secondary meson beam was formed from mesons produced at and near 0 deg. The thickness of polyethylene was empirically determined to give the maximum number of pions of 250 MeV kinetic energy down the pion beam channel.

The greater part of the mesons in the secondary beam was produced via the reaction $p + p \rightarrow \pi^+ + d$. At a given angle, these mesons are produced with a unique energy depending only on the energy of the incident proton. The specific ionizations of the protons and pions involved are such that, roughly speaking, a meson emerges at the downstream end of a polyethylene target with an energy that is independent of where in the target the reaction took place. The optimization of the production target therefore consisted in finding the thickness such that all pions produced by the reaction $p + p \rightarrow \pi^+ + d$ at 0 deg emerge with a kinetic energy of 250 MeV. The rest of the mesons were produced by the inelastic processes $p + p \rightarrow \pi^+ + p + n$ and $p + n \rightarrow \pi^+ + n + n$.

The magnet system used for momentum analysis and focusing of the pion beam is shown in Fig. 19. It was designed by Dr. R. A. Swanson,[20] and was set up and in use fairly continuously during the years 1961-63 in a number of experiments requiring intense beams of low-energy pions or muons. It is a double-focusing system, and combines the usual advantage of double-focusing systems (no momentum dispersion at the second focus) with an unusually short flight path and a large aperture for the pions. The total flight path of the pions was 30 feet, roughly half the length of more conventional double-focusing systems. This is important because of the short mean decay length of pions at this momentum (65 ft).

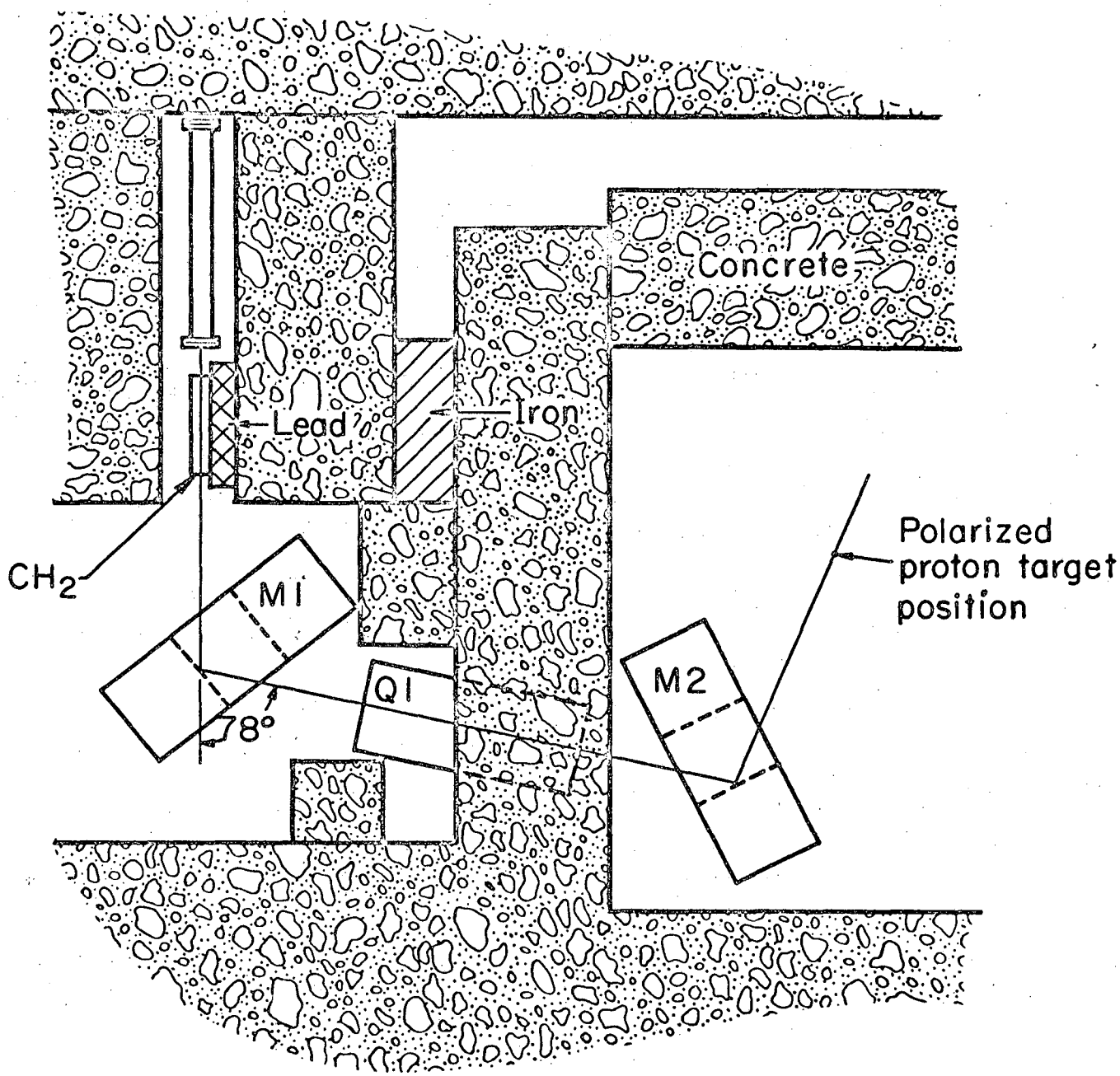

Fig. 19. Plan view of the pion beam transport system.

MU-32814

The magnet system consisted of two bending magnets, placed symmetrically on each side of a symmetric three-element quadrupole. The bending magnets had a vertical aperture of 7-5/8 in. The entrance and exit quadrupole elements had 12-in. apertures; the center section had a rectangular aperture 16 in. wide and 6.5 in. high. The entire length of the pion beam from the production target to the exit of the second bending magnet was enclosed in a vacuum system.

There was a horizontal and vertical focus at the center of the quadrupole triplet. The vertical focusing was achieved entirely by the bending magnets. This was possible because of the large angle of bend in each magnet (78 deg), which caused the particles to pass through the entrance and exit fringe fields at a steep angle. The horizontal focusing was achieved by the end sections of the quadrupole triplet. The center section acted as a field lens in the vertical plane.

A horizontal collimator was placed at the first focus to determine the momentum bite and eliminate stray particles from the beam. The jaws of the collimator were 2-in.-thick lead; this degraded pions passing through it sufficiently to prevent them from passing through the second half of the beam optics system. In the collimator was placed a 1-in.-thick piece of polyethylene; this degraded protons of the right momentum formed in inelastic collisions at the production target and prevented them from reaching the second focus.

The width of the collimator was 2 in. during most of the experiment. The energy spread of the beam was approximately ± 3% at half maximum. The mean energy was 246 ± 1 MeV. (This is actually the calculated value of the

mean beam kinetic energy at the center of the target. The mean energy before the target was slightly higher.) This was determined by measuring the range distribution of beam particles at the second focus in copper moderator.

Beam profiles were taken at the second focus with two small overlapping, remotely maneuvered counters. Full width at half maximum was 2.2 in. in the horizontal direction, and 1.5 in. in the vertical.

Approximate values for the magnet currents were obtained by extrapolation from currents found to be suitable in a previous experiment with pions of nearly equal momentum.[19] The current in the second bending magnet, M_2, was optimized by requiring that pions of the desired energy be projected from the center of the collimator at the first focus to the second focus. This was determined by taking beam-range curves at various currents. The current in the first bending magnet, M_1, was optimized so as to bring pions of the desired momentum to the center of the collimator. This was determined by requiring that the beam at the second focus be centered on the surveyed beam center line (that is, on the line of 78 deg bend in M_2). The current in the end sections of the symmetric quadrupole triplet was determined by minimizing the horizontal width of the beam at the second focus, as measured by the beam-profile technique discussed above. An attempt was made to optimize the current in the field lens by maximizing the beam intensity at the second focus. However, the optimum current turned out to be greater than the maximum current permitted in that magnet, because of coil heating. Since the beam intensity was not very sensitive to the field lens current, the field lens was used with the maximum safe

current.

The pion beam intensity at the second focus is estimated to have been approximately 3×10^6 per second, of which about one-third struck the target. The beam was contaminated with a few per cent muons and electrons,[19] but since these do not affect asymmetry measurements of the type performed in this experiment, no measurement of the beam composition was made.

The Berkeley synchrocyclotron has an auxiliary dee[21] that can be used to stretch the beam spill to about 12 msec (out of the 16.7 msec of the acceleration cycle). However, the 54-nsec rf structure is still present. The stretched beam spill was used throughout the experiment, with a consequent improvement in duty cycle by about a factor of 50.

The pion-production target and the first half of the magnet system were completely enclosed by a concrete blockhouse with walls about 5 ft thick in order to reduce the amount of stray radiation in the region of the particle detectors near the polarized target. The primary proton beam that passed through the pion-production target was deflected slightly in M_1 and buried in a 3-ft-deep well in the rear of the blockhouse. Additional shielding of concrete, iron, and lead was placed in critical areas, such as along the direct line of flight between the production target and the particle detectors.

During part of the experiment it proved desirable to reduce the beam energy spread (see Section IV.F.3). The collimator at the first pion-beam focus was narrowed to 3/4 in. Magnet currents were re-optimized according to the criteria discussed above. With this collimator, the beam energy

spread was ± 2% full width at half-maximum. The beam intensity was lower by about a factor of 2 than with the 2-in.-wide collimator. Since the polarized target and associated apparatus were in place during the time when the narrow collimator was used, no beam profiles at the second focus were taken.

C. Counters and Electronics

The scattered pions were detected by the scintillation counter π_1, which was mounted on a cart and could be moved on a pair of rails along the arc of a circle of radius 22-1/4 in. concentric with the target. The recoil protons were detected by five fixed scintillation counters $P_1 \ldots P_5$. Immediately behind these was counter P_c ("P common"), which was large enough and so positioned that any particle traveling from the target to one of the counters $P_1 \ldots P_5$ would pass through it. Its purpose was to reduce accidental counts due to random photomultiplier-tube noise by requiring scattering events to register as threefold instead of twofold coincidences.

For the angles at which the recoil protons could not be detected, a differential range telescope was used to detect the scattered pions. The telescope is shown in Fig. 20. To be registered as having scattered off a free proton, pions had to pass through π_1 and R_1 but not through R_2.

A U-shaped anticoincidence counter was placed immediately upstream from the cryostat, at the level of the target. Figure 21 shows the shape of the counter as the beam sees it; it is called the "Arc de Triomphe." Its purpose was to give a veto signal for scattering events originating in the thick metal parts of the cryostat.

Two counters, called L and R, were placed 21 in. upstream from the target on the left and right side, respectively, and were used to monitor

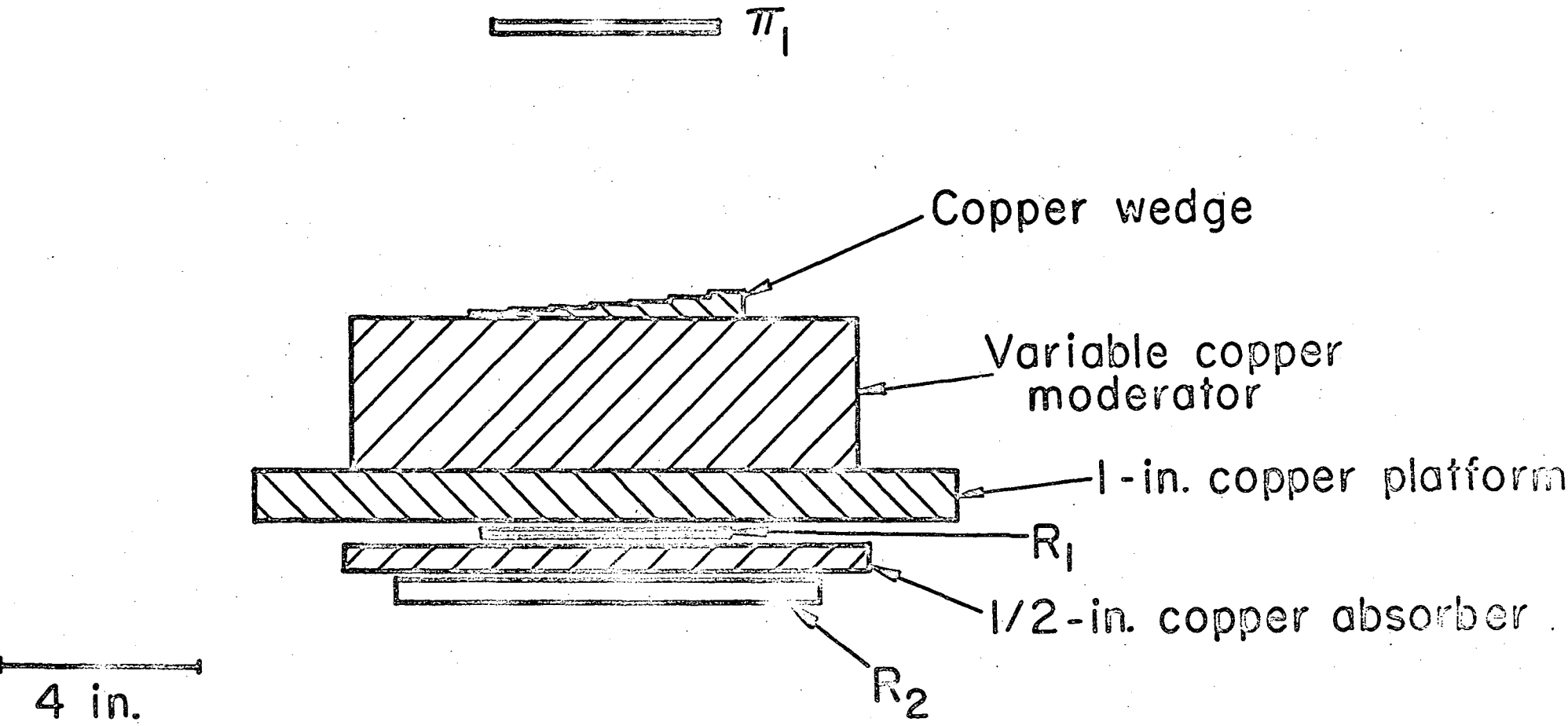

Fig. 20. The scattered-pion range telescope.

MU-32813

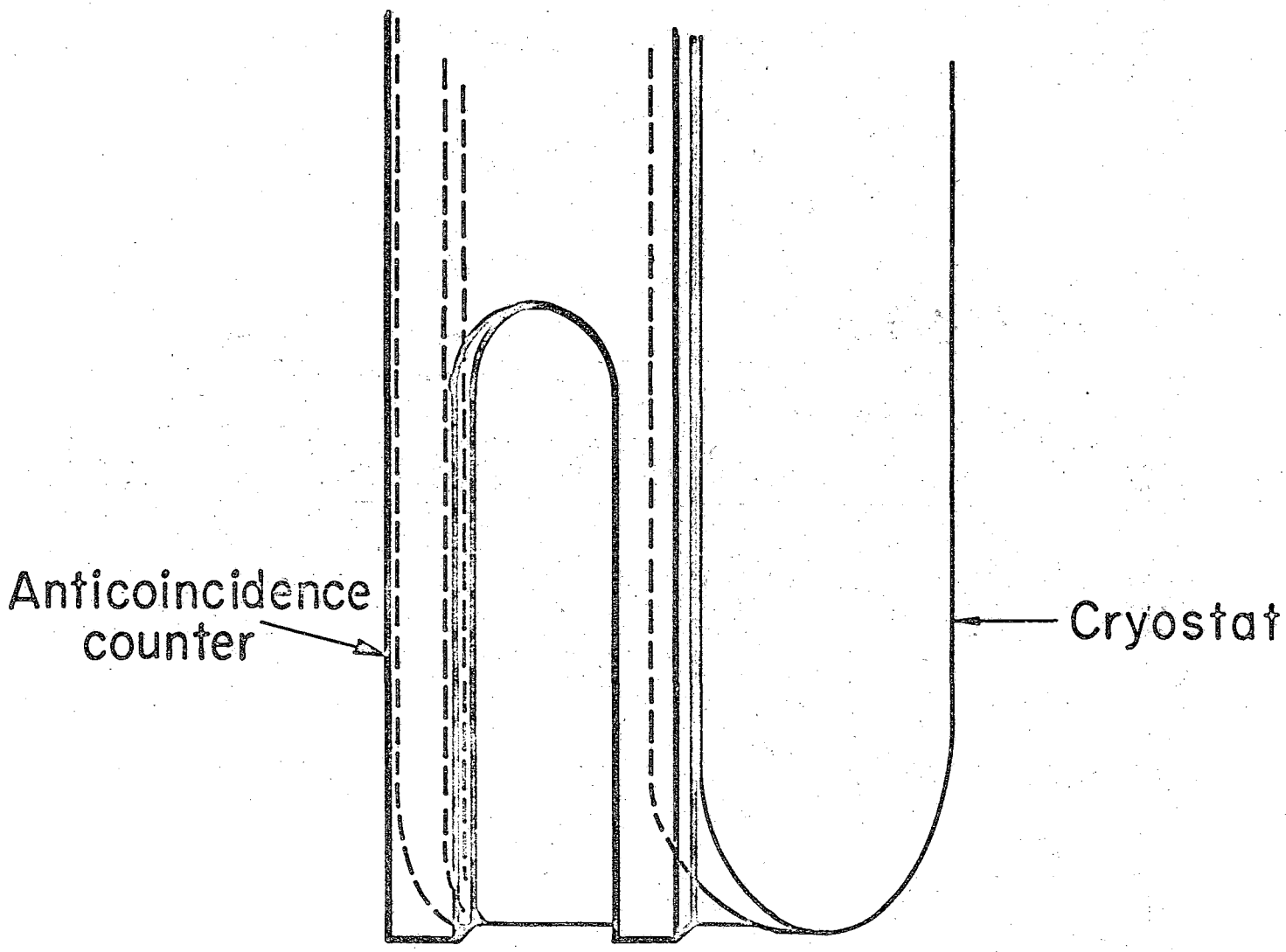

Fig. 21. The "Arc de Triomphe" anticoincidence counter, shown in position upstream from the cryostat.

MU-32815

the horizontal beam position (see Section IV.F.2).

When desired, the counter telescope for measuring the range of the beam particles could be installed on a platform upstream from the target.

Each counter was made of a solid solution of terphenyl in polystyrene, the standard Radiation Laboratory scintillator material, and was viewed through a solid lucite light pipe by a RCA-6810 photomultiplier tube. The dimensions of the scintillating region of each counter, as well as other pertinent information, are given in Table I.

The signal from each of the pion and proton counters was passed through a tunnel diode voltage discriminator,[22] delayed, split when necessary by an "active splitter" with an approximate voltage gain of 1,[22] and fed into coincidence circuits of the Wenzel type.[23] The outputs of the various coincidence circuits were passed through discriminators and fed into scaling units.[22] The outputs of the A, L, and R counters were similarly treated, but their singles counting rates were so high that they could not be passed through the tunnel diode discriminators.

D. Logic

A schematic diagram of the electronic logic is shown in Fig. 22. The pulses from the counters π_1, P_c, and A were split and placed into coincidence circuits with pulses from each of the counters $P_1 \cdots P_5$. When π_1 was in a position to count pions conjugate to the protons in P_i, the π-p events were registered by the coincidence $\pi_1 P_i P_c \bar{A}$ (a bar over the counter name means that the counter was connected in anticoincidence). At the same time coincidences $\pi_1 P_j P_c \bar{A}$ $(P_j \neq P_i)$ were scaled, to gain information on the background at angles not conjugate for scattering from free protons.

Figure 22 also shows the logic used to identify the π-p events at angles where the recoil proton was not detected. In this case a π-p event was registered by the coincidence $\pi_1 R_1 \bar{R}_2 \bar{A}$.

Table I. Characteristics of counters used in asymmetry measurement.

Counter	Width in the θ direction (in.)	Width in the ϕ direction (in.)	Thickness (in.)	Distance from target (in.)
P_1	1.5	1.5	1/4	48
P_2	1.5	1.75	1/4	48
P_3	1.5	2	1/4	48
P_4	1.5	2.25	1/4	48
P_5	1.5	2.5	1/4	48
P_c	16	2 to 3 (flared)	1/4	49
π_1	4.5	4.5	1/4	22.25
R_1	5	5	3/16	32
R_2	9-in. diameter		1/2	33

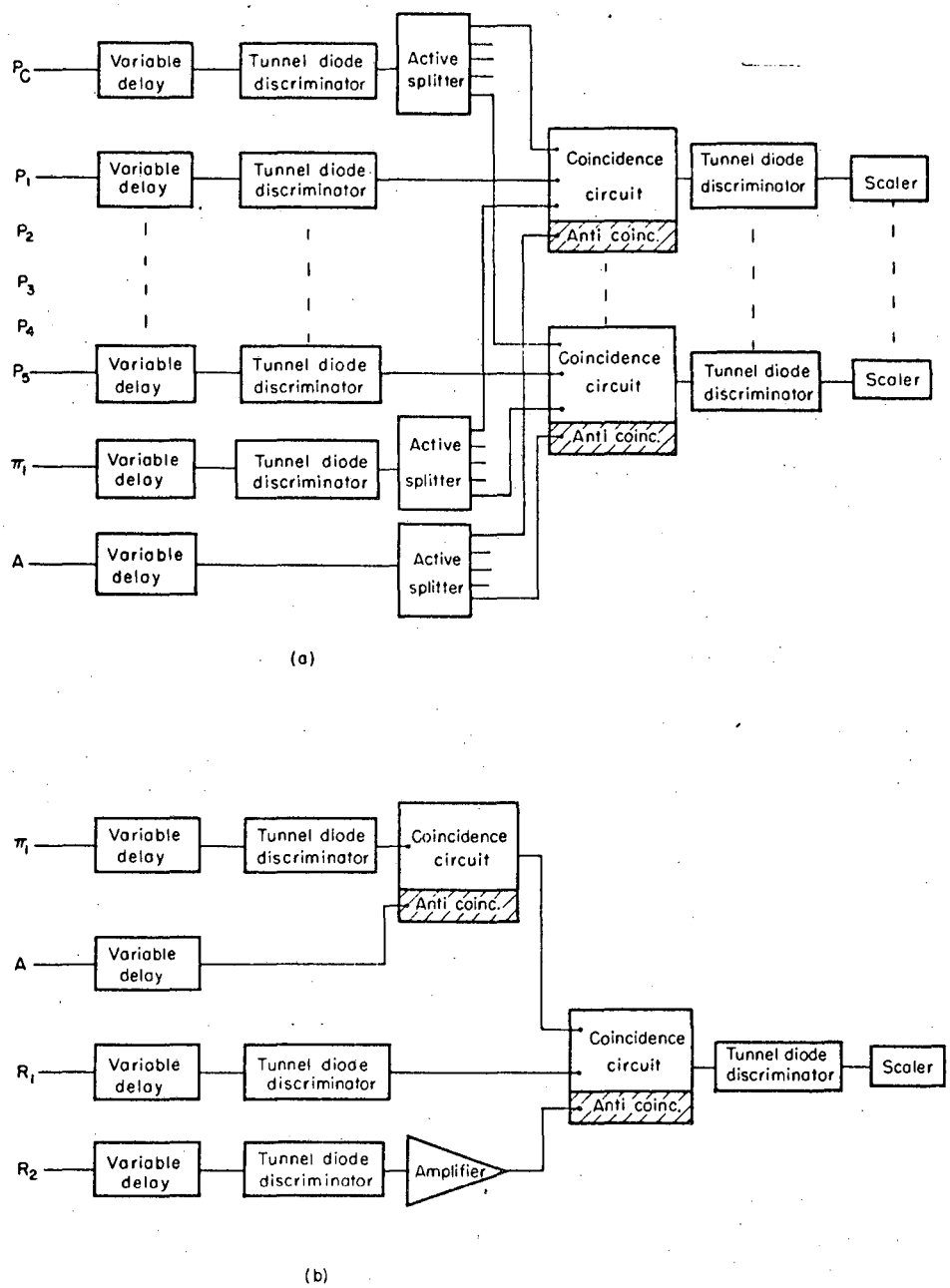

Fig. 22. Schematic diagram of the logic used to identify elastic events: (a) pion-proton angular correlation; (b) pion angle-range correlation.

MUR-2275

E. Normalization of Counting Rates

The pion beam intensity was monitored by a 2-in.-deep argon-filled ionization chamber of the type commonly used at the Radiation Laboratory[24] placed at the exit face of the second bending magnet. The current from the chamber was integrated by an electrometer, the charge stored in a 0.00936-μF capacitor, and the voltage across the capacitor was continuously monitored by a voltmeter and displayed on a pen recorder. The integrated beam current thus displayed was used to normalize all counting rates.

F. Experimental Procedures

1. Beam Monitoring

The steps followed in the initial optimization of the pion beam in terms of intensity, energy, position, and sharpness of focus and direction have been described in Sec. IV.B.

At several hours' intervals during data taking, the position of the primary proton beam was checked by exposing an x-ray film to it just upstream from the meson-production target in a reproducible location. An exposure of 1/10 sec at full beam intensity (5×10^{11} protons per sec) proved satisfactory.

The position of the pion beam was also checked every few hours by exposing an x-ray film to it just downstream from the polarized target. The outline of the target crystals could be faintly seen on the developed films, so that the centering of the beam on the target could be checked directly. A representative picture is shown in Fig. 23. An exposure time of about 10 min was satisfactory.

A number of auxiliary counters and circuits were used in the experiment to monitor the pion beam position and duty cycle.

A scintillation counter was placed close to the rear wall of the blockhouse enclosing the meson production target, but well out of the primary proton beam. Its output, displayed on a slow oscilloscope triggered by a signal from the cyclotron dee voltage, provided a convenient monitor of

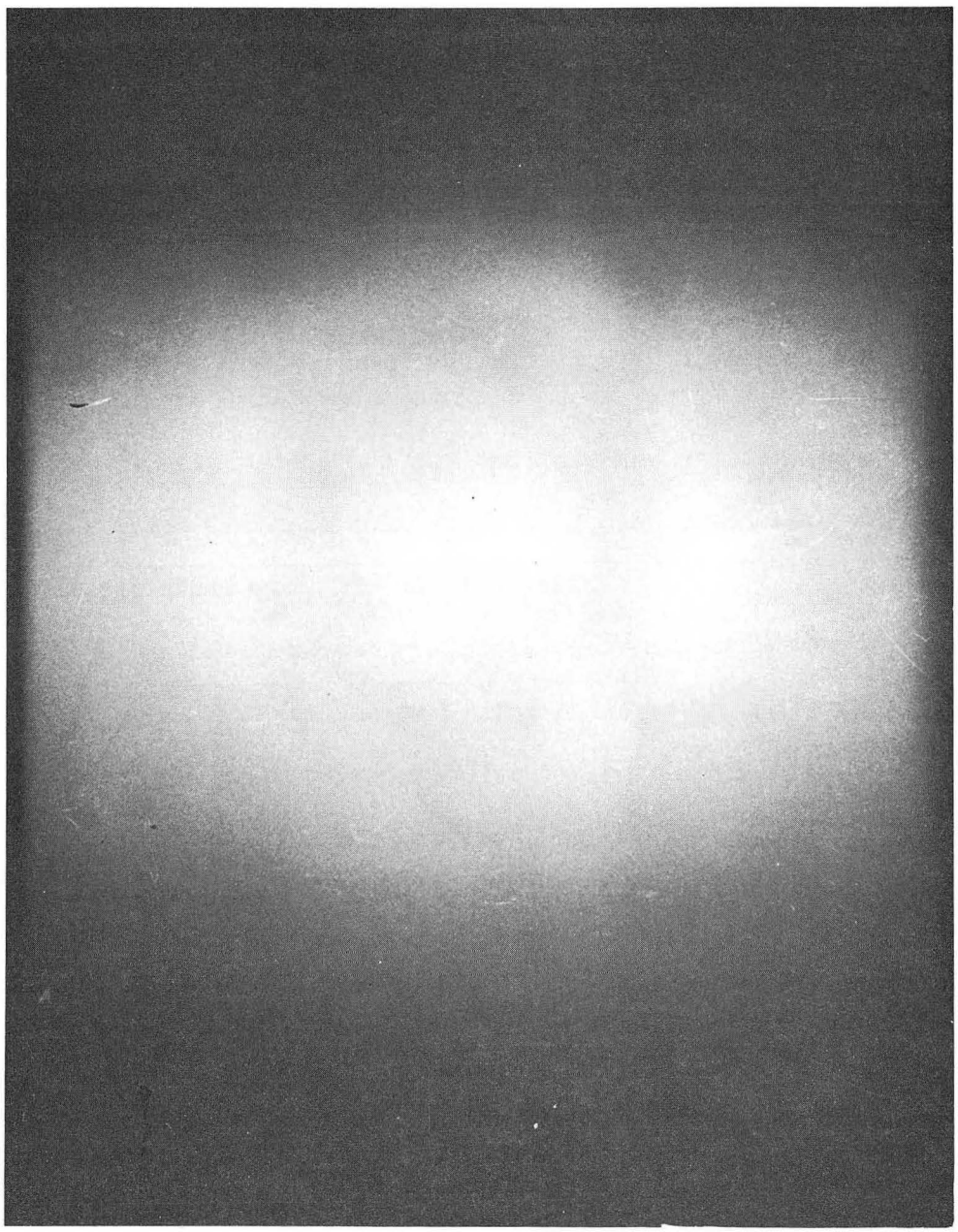

ZN-4157

Fig. 23. Outline of the target crystals as seen on x-ray film exposed to the pion beam immediately in back of the cryostat.

the beam duty cycle.

A monitor of the instantaneous beam rate was obtained by scaling twofold coincidences between pulses from the dynode of the "Arc de Triomphe" counter, one of which was delayed by 53 nsec. This interval is the period of the cyclotron's rf structure, and accidental coincidences such as the ones scaled by this circuit are maximized by delaying one pulse by an integral multiple of 53 nsec.

At various times during the experiment the coincidence counting rates $P_cP_1\overline{A}$, $P_cP_2\overline{A}$, and $P_cP_5\overline{A}$ were used to center the pion beam on the target horizontally. An attempt was also made to use these rates as monitors of the horizontal beam position. (The ionization chamber, being 6 feet upstream from the target, was not sensitive to shifts in the beam position.) However, these circuits showed a target-polarization dependence of a few tenths of a percent in counting rate, owing partly to the small change in the magnetic field of Pia when reversing polarization and partly to the small fraction of polarization-dependent π-p events, and were therefore of little use.

A very sensitive monitor of the horizontal beam position was provided by the two counters L and R, placed 21 in. upstream from the target to the left and right side of the beam respectively, in the regions where the beam intensity varied most steeply with transverse position. As the beam position shifted to one side, the counting rates in L and R changed in opposite directions, so that the ratio of counting rates L/R was extremely sensitive to the horizontal beam position. A shift of 0.1 in. could easily be detected.

2. General Procedures

The voltages to which the counters were set, the delays of the individual counter pulses before reaching the coincidence circuits, and the

settings of the various discriminators were determined by observing the appropriate coincidence counting rates as functions of these parameters. Although preliminary settings were determined by using light pulsers, the final settings were determined under conditions identical to those during data taking.

The accidental counting rates, due both to beam particles and to cosmic radiation, were found to be negligible. The effect of variations of the instantaneous beam rate on the normalized counting rates was also negligible.

3. Procedures at Individual Angles

The positions of the proton counters $P_1 \cdots P_5$ were chosen on the basis of rough preliminary calculations of the particle orbits in the field of Pia. The c.m. angles were chosen so as to divide the experimentally accessible angular region into five equal subregions. The position of π_1 conjugate to each of the counters $P_1 \cdots P_5$ was empirically determined by maximizing the appropriate coincidence counting rate. A typical plot obtained in this fashion is shown in Fig. 24.

At position 1 (θ = 147.0 deg), a peculiar background problem was encountered. Some of the beam particles were scattered by π_1, which because of the bending effect of Pia was close to the incident beam, and registered in P_1, giving an apparent π-p event. Since these fast mesons had a much lower specific ionization than the recoil protons, the background was eliminated by raising the discriminator level of P_1.

The differential range telescope used to identify π-p events at the two smallest c.m. angles was positioned on the basis of rough preliminary calculations of the pion orbits in the field of Pia.

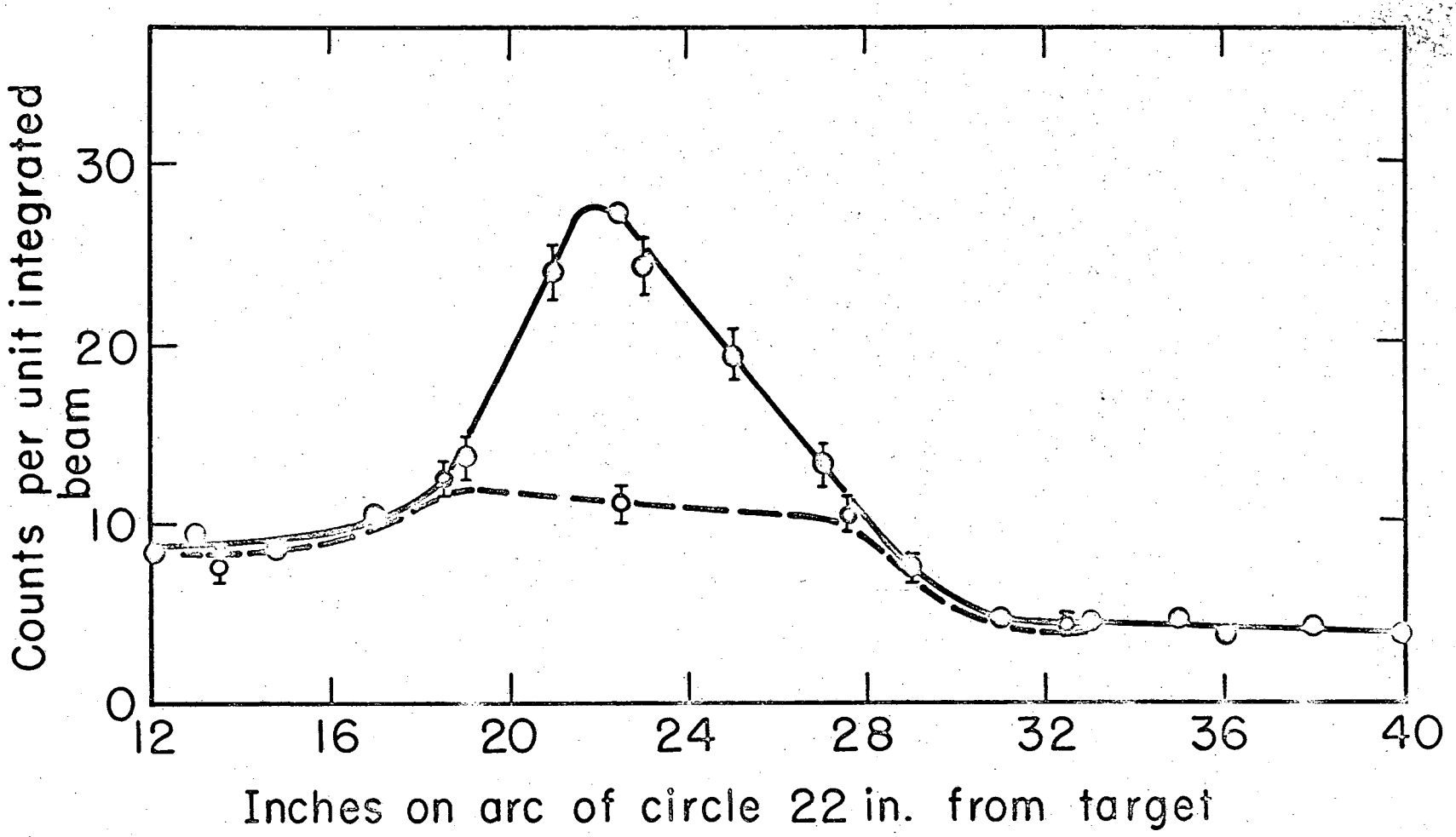

Width of counter

Fig. 24. Pion-proton councidence counting rates vs pion counter position for proton counter angle 129.1 deg c.m. Solid points taken with crystal target, open points with dummy target. Curves are drawn to connect the points and have no further significance.

MU-29816A

At these two angles, the background due to scattering on bound nucleons was considerably reduced by reducing the energy spread of the beam, thus making the pions scattered from free protons more nearly mono-energetic. This was achieved by reducing the horizontal collimator width at the first focus of the meson beam from 2 in. to 3/4 in.

The upper and lower limits on the range of the accepted particles were determined by varying the thickness of copper moderator between π_1 and R_1. A 1/8-in.-thick piece of copper was always between R_1 and R_2 to increase the counting rate $\pi_1 R_1 \bar{R}_2 \bar{A}$. A differential range curve thus obtained is shown in Fig. 25. The slight rise in counting rate in the vicinity of 60 g/cm^2 variable moderator is due to pions elastically scattered on hydrogen. Asymmetry data were taken with an amount of variable moderator such as to maximize the fraction of π-p events.

4. Asymmetry Measurements

The counting rate of elastic π-p events at a given angle was measured with alternate directions of the target polarization. The polarization was reversed every 1.5 to 2 hours. In order that the beam and electronic circuits could be periodically checked, the counts in the various circuits were recorded every 15 to 30 minutes, each such division of the data being known as a "run." The target polarization was continuously monitored in the way described in Section II.C.4. The beginning and end of each run were marked on the recorder chart containing the record of the target polarization, so that an average polarization could be accurately calculated for each run.

5. Background

Referring to Fig. 24, one sees that under the assumption that the background of bound-nucleon events is not strongly angle-dependent this background can be estimated from the counting rates at positions well

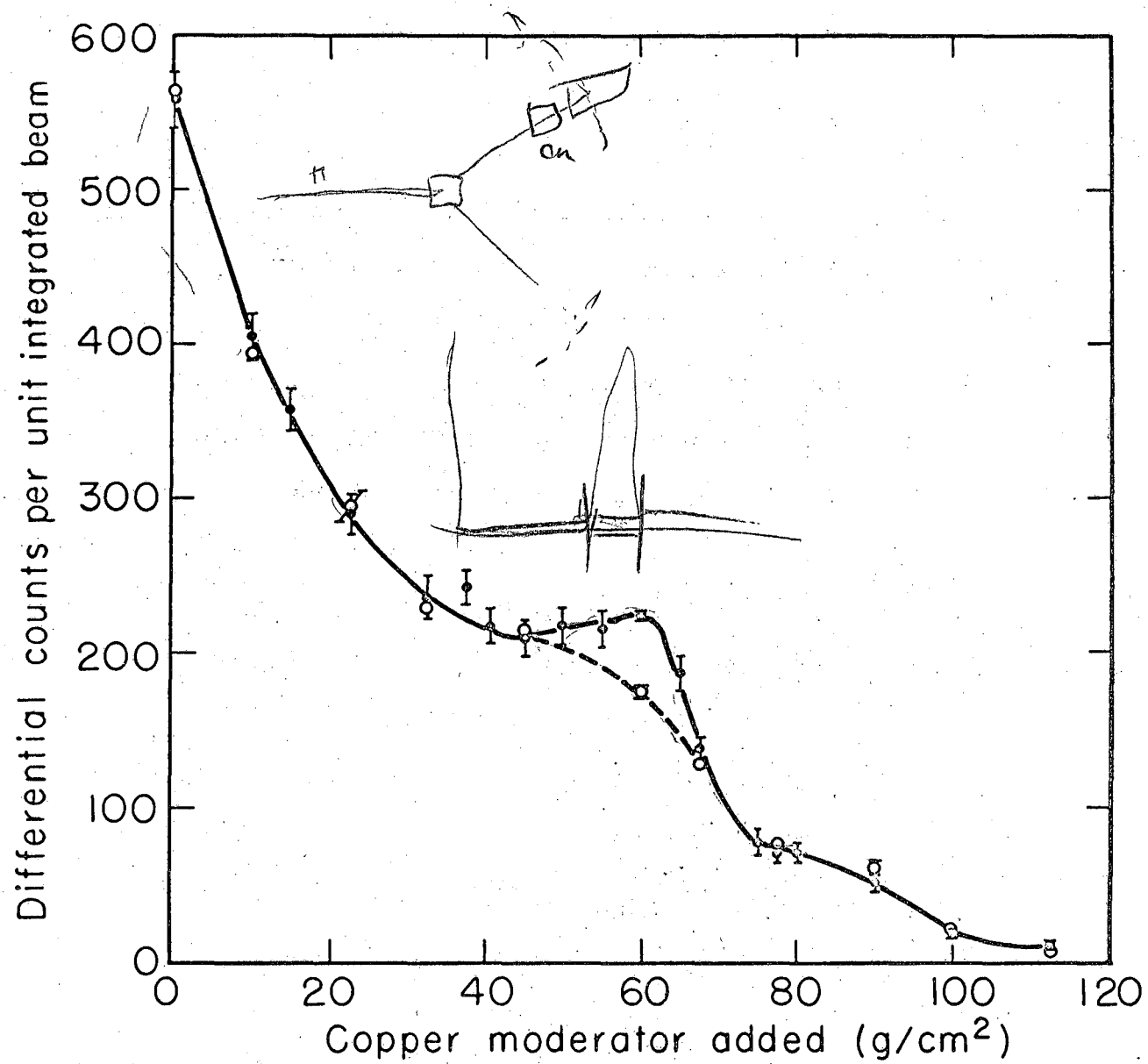

Fig. 25. Scattered pion differential range telescope counting rates vs amount of copper moderator at θ = 68.0 deg c.m.; solid points taken with crystal target, open points with dummy target. Curves are drawn to connect the points and have no further significance. Horizontal scale is in variable g/cm^2 added to a fixed amount.

MU-29815A

away from the free-proton peak. The background at the position of the free-proton peak appears to comprise about 40% of the total counting rate.

To check on this estimate, a dummy target was constructed and substituted for the crystal target. The dummy target had the same weight as the crystal target, and roughly the same composition in terms of heavy and light elements. It was a mixture of barium carbonate, magnesium carbonate, and teflon: barium to take the place of lanthanum, and carbon, oxygen, and fluorine to take the place of nitrogen and oxygen in the crystal target. It was baked out and thereafter stored in a desiccator, to ensure that it contained no water. The dummy target was placed in a replica of the microwave cavity and positioned identically as the crystal target inside the cryostat. In order to simulate as closely as possible the conditions of data taking, the dummy target was immersed in liquid helium in the cryostat.

Figure 24 shows an example of the counting rates as a function of pion counter position in one of the coincidence channels intended to count π-p events, both with the real and the dummy target. Figure 25 shows differential range curves taken at $\theta = 68.0$ deg with the real and dummy target.

In both Figs. 24 and 25 a slight rise in counting rate from the dummy target can be observed in the regions where elastic π-p events would be expected to occur. This rise is due to scattering from the hydrogen in the Mylar liguid helium container and in the Mylar window of the vacuum can that surrounds the target. Data taken with the target removed but the cryostat in place confirm this explanation.

V. CALCULATIONS

A. Background Subtraction

Although the polarized target and the dummy target were of equal weight, the volume of the dummy target was roughly 1/3 greater. Thus the dummy target presented fewer g/cm^2 to the beam, but intercepted a larger area of the beam; also the counting geometry was slightly different. There was no *a priori* reason to expect the background counting rates to be equal in the two targets. Rather, one might have expected to find curves of *similar shape* when joining the points in Figs. 24 and 25 in the regions where no π-p events are expected to occur, with absolute counting rates somewhat different. However, it turned out that the counting rates from the polarized target and the dummy target were equal within the statistical errors in all cases where no elastic π-p events were expected. Consequently, the quantitative determination of the background was made in a straightforward manner, comparing counting rates from the polarized and dummy targets under otherwise identical conditions. The quantity that enters into the calculation of the polarization in π-p scattering is the fraction f of true elastic π-p events from the crystal target among the total events accepted as such by the logic. This quantity was calculated from the equation

$$f = \frac{\text{Counting rate from polarized target} - \text{Counting rate from dummy target}}{\text{Counting rate from polarized target}} \qquad \text{(V-1)}$$

for each of the seven angles. The counting rate from the polarized target was taken to be the average of the counting rates for the two orientations of the target polarization. Since these counting rates were used in calcu-

lating the scattering asymmetry, they were measured with relatively good statistical accuracy ($\approx 0.6\%$), so that the uncertainty in the values of f comes mainly from the statistical errors of the counting rates from the dummy target. Typical values of f were 0.5 when the pion-proton coincidence method was used, and 0.2 when the range telescope was used to identify π-p events.

B. Calculation of the Polarization in Elastic π-p Scattering

1. Formulae and General Procedures

The counting rate of events accepted by the logic as π-p events at any angle can be written

$$R_{\pm} = R_0(1 \pm \epsilon), \tag{V-2}$$

where the plus sign stands for the rate with the target polarization parallel to the unit vector $\hat{n}$ of Eq. (III-10), and minus sign for antiparallel; R_0 is the counting rate when the target is unpolarized; and ϵ is the "raw asymmetry". Solving Eq. (V-2) for ϵ gives

$$\epsilon = \frac{R_+ - R_-}{R_+ + R_-} . \tag{V-3}$$

Recalling Eq. (III-15) for the differential scattering cross section of pions from a polarized proton target in the absence of any background,

$$I(\theta) = I_0\ (\theta)\ (1 + \vec{P}_T \cdot P\hat{n}), \tag{III-15}$$

one can generalize this to include the background,

$$I(\theta) = I_0(\theta)\ (1 + \vec{P}_T \cdot P\hat{n}) + I_B(\theta), \tag{V-4}$$

where I_B is the intensity of background particles. Rewriting this in terms of counting rates in a specific geometry results in

$$R(\theta) = \mathcal{F}_0(\theta)\ (1 + \vec{P}_T \cdot P\hat{n}) + B(\theta), \tag{V-5}$$

$$R_\pm = \mathcal{F}_0\ (1 \pm \vec{P}_T\ P) + B, \tag{V-6}$$

where $\mathcal{F}_0$ is the counting rate from the unpolarized free protons in the target, B is the background counting rate.

Substituting Eq. (V-6) into Eq. (V-3) one has

$$\epsilon = \frac{\mathcal{F}_0\ P_T \cdot P}{\mathcal{F}_0 + B} = \frac{\mathcal{F}_0}{R_0}\ P_T \cdot P = fP_TP; \tag{V-7}$$

$$P = \frac{\epsilon}{P_T \cdot f}\ . \tag{V-8}$$

Equation (V-8) was used to calculate the π-p polarizations.

At each angle, the average counting rates R_+ and R_- were used to calculate an average asymmetry ϵ . The target polarization was calculated by averaging the absolute values of the polarizations of the individual runs, weighted by the duration of the runs in units of integrated pion beam intensity.

The procedure desribed above is clearly an approximation, for it lumps all the data together and makes no attempt to observe any variation of ϵ with $|P_T|$. However, the fractional error of ϵ due to statistics was so large, and the variation in $|P_T|$ so small, that the approximation is quite justified. As a test, the data at $\theta = 108.4$ deg were analyzed in a more correct way, weighting the result of each run by the magnitude of the target polarization. (This angle was chosen because there were unusually large variations in $|P_T|$.) The resulting value of the π-p polarization agreed with that obtained by the simpler analysis to within 1 part in 200.

Typically, at each angle, 20 runs were taken with each sign of target polarization. The polarization was reversed approximately eight times, and data at each angle were taken on at least two different days. As a test of internal consistency the data at each angle were divided into approximately four groups, containing roughly equal amounts of data with positive and negative target polarization taken in immediate time sequence, and the asymmetry was separately calculated for each group. No unduly large deviations from the average asymmetry were observed.

2. Sample Calculation

To illustrate the description of the method of calculation of the π-p polarization, and to point out the principal difficulties and sources of error, the essentials of the calculation for counter position 1($\theta = 147.0$ deg) are reproduced in this section.

The unit of integrated beam intensity to which the counting rates are normalized is 1 V on the integrating electrometer mentioned in Sec. IV.E.

This corresponds to a total flux of about 4×10^7 pions passing through the target. A total of 34 runs of 20 integrated volts each were made at this angle on two successive days, 18 runs with positive and 16 with negative enhancement of the target polarization. The 34 runs were divided into four groups, consisting of several runs with each sign of target polarization taken in immediate time sequence.

The normalized counting rates in the various coincidence circuits are given in Table II. The raw asymmetry in $\pi_1 P_c P_1 \bar{A}$ as defined by Eq. (V-3) is computed separately for each group of runs. The field direction of Pia was such that the target polarization was parallel to $\hat{n}$ at negative enhancement. Therefore, in Eq. (V-3), R_+ is the counting rate for negative enhancement, and R_- the counting rate for positive enhancement. The scatter in the values of the raw asymmetry is roughly as expected from the errors on the individual values. The cumulative average counting rates and the raw asymmetry in $\pi_1 P_c P_1 \bar{A}$ are computed, and show a definite effect due to the target polarization. The other coincidence rates $\pi_1 P_c P_i \bar{A}$ $(i \neq 1)$ show no such effects.

Letting T stand for the counting rate in $\pi_1 P_c P_1 \bar{A}$ when the target is unpolarized, and B for the counting rate from the dummy target, the fraction f of elastic hydrogen events in $\pi_1 P_c P_1 \bar{A}$ is, from Eq. (V-1),

$$f = \frac{T - B}{T} , \qquad \text{(V-9)}$$

where T is taken to be the average of the counting rates for negative and positive enhancement. From the values in Table II,

Table II. Average normalized counting rates and asymmetries at θ = 147 deg.

	Enhancement	Volts (integrated)	Coincidence counting rates					ϵ
			$\pi_1 P_c P_1 \bar{A}$	$\pi_1 P_c P_2 \bar{A}$	$\pi_1 P_c P_3 \bar{A}$	$\pi_1 P_c P_4 \bar{A}$	$\pi_1 P_c P_5 \bar{A}$	
Group 1	Negative	(80)	30.375±0.617	16.588±0.456	10.763±0.367	7.300±0.302	5.600±0.265	-0.0108±0.0143
	Positive	(80)	31.038±0.623	16.213±0.454	10.288±0.364	7.725±0.304	4.850±0.263	
Group 2	Negative	(60)	30.617±0.716	16.517±0.516	10.100±0.401	7.750±0.364	4.633±0.289	-0.0311±0.0162
	Positive	(60)	32.583±0.738	15.383±0.507	9.600±0.400	7.900±0.364	4.950±0.289	
Group 3	Negative	(100)	31.610±0.562	16.350±0.405	10.760±0.317	7.680±0.283	5.475±0.241	-0.0085±0.0125
	Positive	(100)	32.150±0.568	16.400±0.405	11.080±0.318	8.080±0.284	5.810±0.242	
Group 4	Negative	(80)	32.213±0.635	16.800±0.459	10.263±0.358	8.288±0.322	5.275±0.257	-0.0118±0.0124
	Positive	(120)	32.983±0.525	17.300±0.380	10.058±0.278	7.517±0.240	4.800±0.200	
Cumulative	Negative	(320)	31.266±0.313	16.553±0.228	10.513±0.200	7.750±0.156	5.287±0.133	-0.155±0.0068
	Positive	(360)	32.253±0.300	16.489±0.214	10.317±0.170	7.783±0.147	5.117±0.119	
Total Cumulative		(680)	31.768±0.215	16.521±0.156	10.415±0.124	7.768±0.107	5.202±0.089	
Dummy target			16.22±1.35	12.89±1.20	7.67±0.93	8.00±0.95	4.55±0.71	

$$f = \frac{31.77 - 16.22}{31.77} = 0.489 \ . \tag{V-10}$$

The rms error in f is given by

$$\begin{aligned} \Delta f &= \left[\left(\frac{\partial f}{\partial T}\right)^2 (\Delta T)^2 + \left(\frac{\partial f}{\partial B}\right)^2 (\Delta B)^2\right]^{1/2} \\ &= \frac{B}{T}\left[\left(\frac{\Delta T}{T}\right)^2 + \left(\frac{\Delta B}{B}\right)^2\right]^{1/2} \approx \frac{\Delta B}{T} \ , \end{aligned} \tag{V-11}$$

where ΔT and ΔB are the rms errors in T and B as given in Table II. Thus, the statistical error of the dummy-target counting rate dominates the error of f. More dummy-target data could have been obtained, but, as is shown later in this section, the error in f contributes a negligible amount to the error on the value of the π-p polarization. Using the values in Table II and Eq. (V-11), one finds

$$\Delta f = \frac{1.35}{31.768} = 0.043 \ . \tag{V-12}$$

The average target polarization is calculated by taking the mean of the polarizations during the 34 runs at this counter position. The latter are calculated as described in Sections II.C.4 and II.C.5. When the individual runs are of different lengths in units of integrated beam intensity, each run is weighted by its length. The average value of P_T at $\theta = 147.0$ deg was 0.203 ± 0.020 .

The elastic π-p polarization can now be calculated from Eq. (V.8):

$$P = \frac{-0.0155}{0.203 \times 0.489} = -0.156 \ . \qquad \text{(V-13)}$$

The rms error in P is

$$= \left[0.1920 + 0.0100 + 0.0077 \right]^{1/2} \times 0.156 \qquad \text{(V-14)}$$

$$= 0.072 \ .$$

The uncertainty in P is seen to be due almost entirely to the statistical error of ϵ . This situation would appear to have been remediable, since all the data at this counter position were taken in only 10 hours' net beam time. However, as can be seen in Table II, the statistical errors on the counting rates for positive and negative target polarization are 1%. It was not deemed advisable to push beyond this accuracy since the integrated beam normalization is believed to suffer from errors of the same order of magnitude. The real limiting factor in the obtainable accuracy in P is the magnitude of the target polarization. If P_T is doubled, ϵ is doubled (ignoring background), and the error in P for a given statistical accuracy is halved.

C. Calculation of the Scattering Angles

The c.m. scattering angles were calculated with the aid of an IBM 7090 program "PIAKIN" (Pia kinematics) written by Helmut Dost of this Laboratory.[8] PIAKIN calculates the asymptotic trajectory of a particle of arbitrary momentum starting at the center of Pia. It takes as input data the value of the central field and its radial dependence, given as the average value of the

field in 14 annular rings of adjustable inside and outside radii. The radial dependence of the field was measured in the midplane with a rotating-coil fluxmeter.

Since the angles were roughly known from earlier hand calculations, orbits of trial angles were computed and plotted on a full-scale drawing of the scattering geometry, and the exact angles of the counters were found by interpolation. Account was taken of the energy loss of the beam pions in the target before interacting, and similarly of the final-state particles after the interaction.

In this way the c.m. angles were computed separately for the proton counters and for the pion counter in each of its empirically determined conjugate positions. The pion counter angles were found to be systematically larger by 1 to 2 deg than the corresponding proton counter angles. This discrepancy was largely removed by assuming the target to have been 1/2 in. upstream from the center of Pia. The longitudinal position of the cryostat was not measured during the experiment, and a misalignment of 1/2 in. could easily have gone unnoticed. The remainder of the discrepancy is explained by (a) the shifting of the mean c.m. scattering angle of the protons striking counter P_i a few tenths of a degree from the angle of the geometric center of P_i, owing mostly to the change in cross section across the face of the counter, and the consequent shifting of the distribution of conjugate mesons, and (b) by the sloping nonhydrogenous background, which causes another shift of a few tenths of a degree in the pion-counter position of maximum coincidence counting rate.

A detailed numerical calculation, including the effects of multiple

Coulomb scattering, the variation of the rms projected multiple scattering angle across the counter, scattering at points other than the center of the target, beam momentum spread, beam angular convergence, and the variation in cross section across the counter, resulted in a shift of the mean detected scattering angle in counter P_5 of 0.3 deg from the center of P_5. A calculation taking into account only the last of the above effects, assuming a linear variation of cross section with angle, and taking for an effective width of P_5 the experimental full width at half-maximum of the conjugate pion distribution, gives the same result. For all other counters the shift in mean detected scattering angle from the angle of the geometric center of the counter was calculated in the latter way.

The effective width in c.m. degrees of P_5 (the full width at half-maximum of the angular distribution of elastic recoil protons detected by P_5) can be calculated from the known counter size, rms multiple scattering angle, and beam angular convergence, in agreement with the experimentally determined one. The effective widths of the other counters were calculated in the same way. The effective widths of all counters were approximately equal.

In the calculation of the mean c.m. scattering angle for each counter position at which data were taken, the target was assumed to have been 1/2 in. upstream from the center of Pia. The effect of the variation in the cross section over the face of the counter was included in the manner described above. When the mean c.m. scattering angles of a pair of conjugate counters differed (as they generally did by a few tenths of a degree), the average of the two angles was taken as the mean angle for that counter position.

VI. RESULTS AND ERRORS

The experimental results are summarized in Table III, and the π-p polarization is plotted vs c.m. angle in Fig. 26.

At position 7, two separate measurements of the asymmetry were made with slightly different physical setups. The polarization values were combined by weighting each result by the inverse of the square of its error. The rms error in the combined result is $\left[(\Delta P_1)^{-2} + (\Delta P_2)^{-2}\right]^{1/2}$, where ΔP_1 and ΔP_2 are the rms errors of the individual quantities.

The principal source of error is the statistical uncertainty of the raw asymmetry. Although the individual counting rates have low rms errors (1%), the experimental asymmetries are so small (2.5% in the most favorable cases) that the statistical uncertainty is a sizeable fraction of, and sometimes greater than, the asymmetry.

The fractional uncertainty in the target polarization is estimated at ± 15%. Of this, about 5% is correlated error, in the sense that all values of the target polarization and consequently of the absolute value of the π-p polarization move up or down together, and is due to the uncertainty in the correction for the change in the resonance line shape. The other 10% is uncorrelated error, due principally to the uncertainty in the amplitude of the thermal equilibrium signal. Only the uncorrelated error is folded in with the statistical error. In one case (position 7b) an error of 15% was assigned because of additional uncertainty in the amplitude of the thermal equilibrium signal.

The uncertainty due to the background subtraction is given by the statistics on the dummy-target counting rates. The correlated error

Table III. Data and results. The parameter P in π^+-p elastic scattering at 246 MeV.

Position	θ c.m. (deg)	Method of discrimination	Raw asymmetry, ϵ	Average target polarization	Fraction hydrogen counts	P
8	68.0	range telescope	0.0163±0.0068	0.254	0.221±0.045	0.290±0.138
7 a	80.5	range telescope	0.0182±0.0046	0.253	0.179±0.057	0.380±0.126
7 b			0.0149±0.0071	0.217	0.193±0.031	
5	108.4	π-p coincidence	0.0241±0.0061	0.191	0.577±0.059	0.219±0.064
4	119.1	π-p coincidence	-0.0031±0.0066	0.194	0.449±0.052	-0.035±0.075
3	129.1	π-p coincidence	0.0036±0.0074	0.183	0.593±0.041	0.033±0.068
2	138.0	π-p coincidence	-0.0067±0.0061	0.190	0.523±0.042	-0.067±0.062
1	147.0	π-p coincidence	-0.0155±0.0068	0.203	0.489±0.043	-0.156±0.072

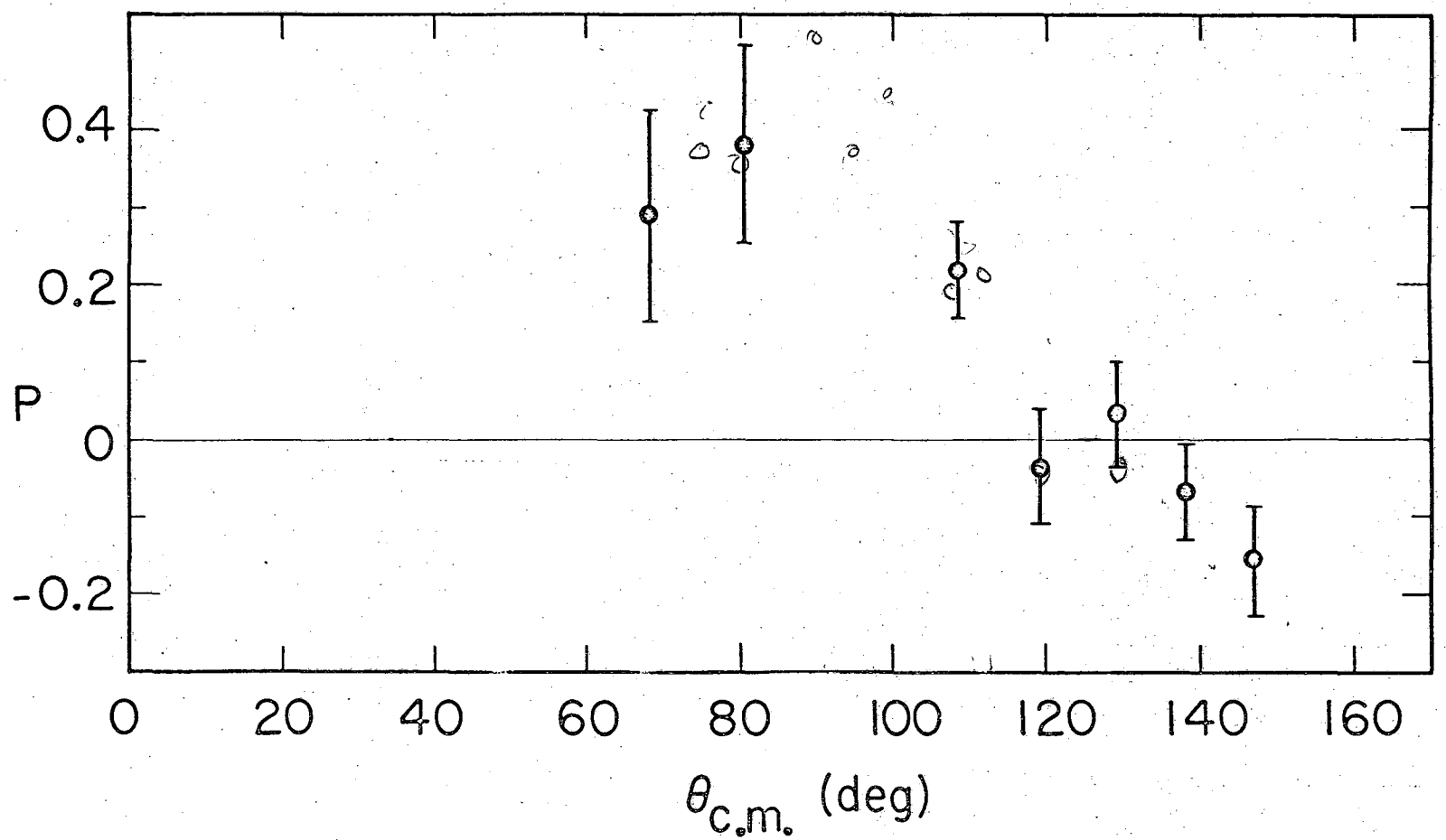

Fig. 26. The polarization parameter P in elastic pion-proton scattering at 246 MeV pion kinetic energy.

MU-32987

resulting from systematically incorrect interpretation of the dummy-target results is estimated to be less than 5%. In one case (position 7a) a slightly larger uncertainty was assigned to f because the background counting rate was estimated from the one measured in position 7b.

A possible source of systematic error was the lateral shift of the beam center at the target during data taking. Because of the careful beam position monitoring described in Sec. IV.F.1, and because the direction of target polarization was reversed at regular intervals, this error is believed to be negligible.

Because of the uncertainty in the exact longitudinal position of the target, the uncertainty in the mean c.m. scattering angle is estimated at $\pm 0.75^{\circ}$.

VII. DISCUSSION OF RESULTS

The results are in qualitative agreement with the polarization results of Foote at 310 MeV;[1] that is, the polarization is small and negative at backward angles in the c.m. frame, and zero near 120 deg. The polarization results at angles smaller than 120 deg indicate that a Fermi-type solution is to be preferred over the various combinations of Minami-and Yang-type solutions (cf. Fig. 6 of reference 1). There already exists strong evidence for this conclusion from the work of Rugge and Vik,[2] simultaneously fitting π^+-p and π^--p elastic scattering and π^--p charge-exchange scattering data. A quantitative study at 246 MeV awaits completion of the analysis of the differential cross section data, which is presently in progress.[19]

Of greater interest is the use of these results combined with accurate data on the π^--p reactions at the same energy, which are yet to be obtained, to give information on the $I = 1/2$ scattering matrix, the parameters of which are far less well known than those of its $I = 3/2$ counterpart.[2]

The availability of a polarized target also brings into the realm of the feasible more complicated experiments such as a measurement of the rotation parameters,[25] which involve the analysis of the polarization of protons recoiling from a polarized target, and which provide independent information on the scattering matrix <u>via</u> the quantities $|g|^2 - |h|^2$ and $\mathrm{Im}\, g^*h$. These experiments, however, necessitate scattering geometries incompatible with the presence of a small-gap iron-core polarizing magnet such as Pia.

The results of this experiment also indicate that dynamically polarized targets of the type described in this report are a useful tool in a wide

class of elementary-particle scattering experiments. The separation of free-proton events from the background, already adequate in this experiment, can be greatly improved by placing tighter constraints on the kinematics when both particles of a two-body final state can be detected, as well as by reducing the angular convergence and momentum spread of the beam. This has been shown in a recent experiment in proton-proton scattering in the energy range 2 to 6 BeV, using the polarized target.[26] In the best cases, the fraction of hydrogen events in the hydrogen channels was 90%. When only one of the final-state particles can be detected, the background suppression can also be greatly improved, particularly through magnetic momentum analysis correlated with visual detection methods or hodoscopes. The method can be extended to the region of quite small energy transfers. In a brief trial run it was found that with the differential range telescope a hydrogen effect could be detected when the energy loss of the mesons was as low as 20 MeV, with the dummy target used for background subtraction.

Polarized targets usually reduce the number of scatterings required for a certain measurement by one: that is, ordinary double-scattering experiments can be done in one scattering; triple-scattering and spin-correlation experiments in two; and so on. The loss in counting rate due to the "thinness" of the polarized target is usually more than compensated for by the gain due to the need for one less scattering. Polarized targets have the additional advantages that fixed counter telescopes can be used to measure an asymmetry, eliminating the most serious systematic error in the usual asymmetry measurement (spurious asymmetries due to misalignment); and that

the "analyzing power" (the target polarization) is independent of particle energy and scattering angle. This makes polarized targets particularly useful at very high energies (above a few BeV), where analyzing powers generally become small, and in reactions involving hyperons which, though polarized, have small decay asymmetry parameters. In addition, many measurements are possible only with polarized targets.[25,27] It is clear that polarized targets will have a long and useful life in experimental physics.

ACKNOWLEDGEMENTS

My deepest thanks go to Professor Owen Chamberlain, who has guided my research and my academic work during the past four years. It was he who proposed this project to me and outlined its basic features, and he has maintained an active interest in the polarized-target program ever since.

I have greatly enjoyed working together with Professor Gilbert Shapiro. His contribution to the development of the polarized target, in terms of ideas and of plain hard work, was very great.

I wish to thank professor Carson D. Jeffries and his former and present students Peter L. Scott, Thomas J. Schmugge, and Kenneth M. Langley for countless discussions of dynamic nuclear orientation and of the techniques of cryogenics, nuclear and paramagnetic resonance, and for valuable help at several crucial points in the development of the polarized target.

Dr. Ludwig van Rossum contributed greatly to the design and execution of the scattering experiment. For help with the setup and running of the experiment I would like to thank my fellow-students John F. Arens, Frederick W. Betz, Byron D. Dieterle, Helmut E. Dost, and Wladyslaw K. Troka. In addition, I want to acknowledge the contribution of Helmut E. Dost in initiating the crystal-growing program.

I wish to acknowledge several informative discussions with Professor Francis M. Pipkin on the theoretical aspects of dynamic nuclear orientation.

Many of the Radiation Laboratory's support groups contributed to the design and building of the polarized target. In particular, I wish to thank Cedric G. Larson for help with the detailed design of Pia, Ivan Lutz and Robert Sorensen for the design of the Pia regulator, and

Harvey E. Maseck and Edwin F. McLaughlin for help with the design of the cryostat; also Quentin A. Kerns and Robert F. Tusting, who designed and built the rf amplifier, and Stephen R. Smiriga, Donald E. McClure, and Ronald Baughn, who designed and built the lock-in amplifier.

The constant support of the Accelerator Technicians under Louis A. Sylvia and Robert E. Walton and of the Hydrogen Target Group under Rene Bollaert and Raymond Fuzesy was very important in the successful completion of this work. The cyclotron crew under James T. Vale and Lloyd B. Houser provided a good beam under sometimes difficult conditions.

I want to thank Mrs. Patricia Brown and Miss Patricia Carson for the typing of the manuscript, and Miss Carson for her friendship and moral support during the difficult years of this research.

This work was done under the auspices of the U. S. Atomic Energy Commission.

APPENDIX

Calculation of High Target Polarizations From the Measured NMR Signals

At target polarizations of the order of 60%, the presence of nuclear magnetism strongly affects the Q of the parallel-resonant circuit; some of the approximations made in deriving Eq. (II-29) are no longer valid, and a more exact calculation must be carried out. A convenient starting place is Eq. (II-18),

$$\frac{1}{Z} = \frac{1}{R + i\omega L(1 + 4\pi\eta)} + i\omega C, \qquad \text{(II-18)}$$

which, by use of the definition (II-24), becomes

$$\frac{1}{Z} = \frac{1}{(R + \varphi'') + i(\omega L + \varphi')} + i\omega C \ . \qquad \text{(A-1)}$$

Tedious but straightforward algebra results in the expressions (on the assumption that $\omega^2 = 1/LC$)

$$|Z| = \omega L \left[\frac{(\omega L + \varphi')^2 + (R + \varphi'')^2}{(R + \varphi'')^2 + (\varphi')^2}\right]^{1/2} , \qquad \text{(A-2)}$$

$$\frac{\partial |Z|}{\partial H_0} = -\omega L \frac{\left[(\omega L + \varphi')^2 + (R + \varphi'')^2\right]^{1/2}}{\left[(R + \varphi'')^2 + (\varphi')^2\right]^{3/2}} \left[(R + \varphi'')\frac{\partial \varphi''}{\partial H_0} + \varphi' \frac{\partial \varphi'}{\partial H_0}\right]$$
$$+ \omega L \frac{(\omega L + \varphi')\frac{\partial \varphi'}{\partial H_0} + (R + \varphi'')\frac{\partial \varphi''}{\partial H_0}}{\left[(\omega L + \varphi')^2 + (R + \varphi'')^2\right]^{1/2}\left[(R + \varphi'')^2 + (\varphi')^2\right]^{1/2}} \ . \qquad \text{(A-3)}$$

At this point it is necessary to consider relative magnitudes of various terms. From measurements it is estimated that $Q \approx 40$ at 80 Mc/sec, so that

$$\omega L \approx 40\ R. \tag{A-4}$$

From the approximate equation (II-25), one obtains, by differentiating,

$$\frac{d|Z|}{|Z|} \approx \frac{d(R + \varphi'')}{R + \varphi''}\ , \tag{A-5}$$

and therefore,

$$\frac{(\Delta|Z|)_{max}}{|Z_0|} \approx \frac{\varphi''_{max}}{R} \approx \pm\ 0.25\ , \tag{A-6}$$

where $(\Delta|Z|)_{max}$ is the maximum change in $|Z|$ due to the proton resonance. The numerical factor 0.25 in Eq. (A-6) is obtained from typical rf level signals at $P_T' \approx 60\%$. The dispersive component $\chi'(\omega)$ of the nuclear susceptibility can be calculated from the absorptive component by use of the Kramers-Krönig relations. Assuming a single resonance line

$$\chi''(\omega) = K \frac{1}{1 + [T_2(\omega - \omega_0)]^2} \tag{A-7}$$

(where K is a constant), the result is[28]

$$\chi'(\omega) = -K \frac{T_2(\omega - \omega_0)}{1 + [T_2(\omega - \omega_0)]^2}\ . \tag{A-8}$$

Although it is clear that Eqs. (A-7) and (A-8) do not exactly describe the actual line shape (see Fig. 16), they can be used to obtain the approximate relative magnitudes of φ' and R. The maxima of $|\chi'(\omega)|$ are at $\omega - \omega_0 = \pm 1/T_2$, and at these points $|\chi'|$ has the value

$$|\chi'|_{max} = \frac{K}{2} = \frac{1}{2} |\chi''|_{max} . \tag{A-9}$$

Hence the approximate result

$$|\varphi'|_{max} \approx 0.125 R . \tag{A-10}$$

Using the approximate relations (A-4), (A-6), and (A-10), and taking the quotient $\frac{1}{|Z|^2} \frac{\partial |Z|}{\partial H_0}$, one finds that the three highest-order terms are

$$\text{Order } \frac{1}{(\omega L)^2} \frac{\partial \varphi}{\partial H_0} : - \frac{1}{(\omega L)^2} \frac{\partial \varphi''}{\partial H_0} \tag{A-11}$$

[this is the highest-order of the terms obtained in the approximate analysis leading to Eq. (II-26)],

$$\text{Order } \frac{1}{Q} \frac{1}{(\omega L)^2} \frac{\partial \varphi}{\partial H_0} : + \frac{R}{(\omega L)^3} \frac{\partial \varphi'}{\partial H_0} , \tag{A-12}$$

$$\text{Order } \frac{|\varphi'|}{R} \frac{1}{(\omega L)^2} \frac{\partial \varphi}{\partial H_0} : - \frac{1}{(\omega L)^2} \frac{\varphi'}{R} \frac{\partial \varphi'}{\partial H_0} . \tag{A-13}$$

In performing the double integration

$$\int_0^\infty d\omega'' \int_0^{\omega''} d\omega' \quad \frac{1}{|Z(\omega')|^2} \quad \frac{\partial |Z(\omega')|}{\partial H_0} \quad . \tag{A-14}$$

As in Eq. (II-29), the term (A-11) yields the result of Eq. (II-29), i.e., a constant times P_T . The term (A-12) gives, by Eq. (II-28),

$$- \frac{\gamma R}{(\omega L)^3} \int_0^\infty d\omega'' \int_0^{\omega'} d\omega' \frac{\partial \varphi'(\omega')}{\partial \omega'} = - \frac{\gamma R}{(\omega L)^3} \int_0^\infty d\omega'' \, \varphi'(\omega'') = 0 \ , \tag{A-15}$$

since φ' is antisymmetric in $(\omega'' - \omega)$. The term (A-13) can be rewritten

$$\frac{\gamma}{(\omega L)^2 \ R} \int_0^\infty d\omega'' \int_0^{\omega} d\omega' \ \varphi'(\omega') \ \frac{\partial \varphi'(\omega')}{\partial \omega'} =$$

$$= \frac{\gamma}{2(\omega L)^2 \ R} \int_0^\infty d\omega'' \left[\varphi'(\omega'') \right]^2 , \tag{A-16}$$

which can be integrated numerically for any given line shape. For the line shape described by Eq. (A-7) and (A-8), the integrals (II-29) and (A-16) can be calculated exactly, and lead to the result (using also (A-10)

$$\text{correction term (A-16)} = \frac{1}{16} \times \text{leading term (II-29)}. \tag{A-17}$$

Although Eqs.(A-7) and (A-8) do not exactly describe the observed line

shape, the result (A-17) gives a rough estimate of the order of magnitude of the correction term.

It is to be noted that this term is always positive, whereas the leading term is positive for positive enhancement and negative for negative enhancement. Thus the correction term, whose origin is the appearance of a nonnegligible reactive component of the tuned-circuit impedance at high polarizations, has opposite effect for the two signs of enhancement: for positive enhancement, it lowers the value of the polarization calculated from the double integral (A-14) by about 1 part in 16; for negative enhancement it raises P_T by 1 part in 16. At thermal equilibrium, $|\varphi'| \lll R$, and the double integral (A-14) suffices.

There are, in addition to the expressions (A-11) through (A-13), a large number of other terms which are down in magnitude by another factor Q or $\frac{R}{|\varphi'|}$. Their effect on the polarization calculation is expected to be small compared with the uncertainty introduced by the 5% measurement error of the thermal equilibrium signal. Changes in the detection electronics as well as in calculational techniques (e.g., calculation by computer) are needed if the accuracy of the polarization measurement is to be significantly improved.

REFERENCES

1. Ernest H. Rogers, Owen Chamberlain, James H. Foote, Herbert M. Steiner, Clyde Wiegand, and Tom Ypsilantis, Rev. Mod. Phys. 33, 356 (1961).
2. Hugo R. Rugge and Olav T. Vik, Phys. Rev. 129, 2300 (1963); Olav T. Vik and Hugo Rugge, Phys. Rev. 129, 2311 (1963).
3. John C. Caris, Charge-Exchange Scattering of Negative Pions by Hydrogen at 230, 260, 290, 317, and 371 MeV (thesis), Lawrence Radiation Laboratory Report UCRL-9048, March 1960 (unpublished).
4. Roger Hill (University of Chicago), private communication.
5. A. Abragam, M. Borghini, P. Catillon, J. Coustham, P. Roubeau, and J. Thirion, Phys. Letters 2, 310 (1962).
6. R. Schermer, H. Postma, F. J. Shore, C. A. Reynolds, H. Marshak, and V. L. Sailor, Bull. Am. Phys. Soc., Ser. 2, 6, 418 (1961).
7. C. D. Jeffries, Dynamic Nuclear Orientation (Interscience Publishers, Inc., New York, 1963); A. Abragam, The Principles of Nuclear Magnetism (Clarendon Press, Oxford, 1961); and other references quoted therein.
8. Helmut Dost (Lawrence Radiation Laboratory), private communication.
9. Carson D. Jeffries (University of California, Berkeley), private communication.
10. J. Hatton and B. V. Rollin, Proc. Roy. Soc. (London) A199, 222 (1949).
11. A. Abragam, op. cit., p. 78.
12. C. D. Jeffries, op. cit., p. 12.
13. A. Abragam, op. cit., pp. 41, 75.
14. Edson Ruther Peck, Electricity and Magnetism (MeGraw-Hill Book Co., Inc., New York, 1953), p. 397.
15. C. D. Jeffries, op. cit., p. 13.
16. J. Hamilton, The Theory of Elementary Particles (Clarendon Press, Oxford, 1959), p. 375.

17. Ibid., p. 124.

18. Lincoln Wolfenstein, Phys. Rev. 75, 1664.

19. Wladyslaw K. Troka (Lawrence Radiation Laboratory), private communication.

20. R. A. Swanson, G. R. Henry, and G. Schrank, 0.5-BeV/c Beam Transport System, University of California at San Diego preprint (unpublished).

21. Q. A. Kerns, Second Dee Master Oscillator, Lawrence Radiation Laboratory Engineering Note EET-743, Dec. 2, 1960 (unpublished).

22. Lawrence Radiation Laboratory Counting Handbook, UCRL-3307 Rev., Jan. 1959 (unpublished).

23. William A. Wenzel, Millimicrosecond Coincidence Circuit for High-Speed Counting, UCRL-8000, Oct. 1957 (unpublished).

24. O. Chamberlain, E. Segre, and C. Wiegand, Phys. Rev. 83, 923 (1951).

25. Young S. Kim, Phys. Rev. 129, 862 (1963).

26. H. Steiner, J. Arens, F. Betz, O. Chamberlain, B. Dieterle, P. Grannis, M. Hansroul, C. Schultz, G. Shapiro, L. van Rossum, and D. Weldon, Bull. Am. Phys. Soc., Ser. 2, 9, 95 (1964).

27. S. Bilenky, Nuovo Cimento 10, 1049 (1958).

28. C. D. Jeffries, op. cit., p. 14; the last term in the denominator of Eq. (2-13) is negligible (see discussion in Sec. II.C.5) and has been left out.

This report was prepared as an account of Government sponsored work. Neither the United States, nor the Commission, nor any person acting on behalf of the Commission:

A. Makes any warranty or representation, expressed or implied, with respect to the accuracy, completeness, or usefulness of the information contained in this report, or that the use of any information, apparatus, method, or process disclosed in this report may not infringe privately owned rights; or

B. Assumes any liabilities with respect to the use of, or for damages resulting from the use of any information, apparatus, method, or process disclosed in this report.

As used in the above, "person acting on behalf of the Commission" includes any employee or contractor of the Commission, or employee of such contractor, to the extent that such employee or contractor of the Commission, or employee of such contractor prepares, disseminates, or provides access to, any information pursuant to his employment or contract with the Commission, or his employment with such contractor.